

Modeling of Power Amplifier Distortion in MIMO Transmitters

Master's Thesis in Wireless, Photonics and Space Engineering

XAVIER BLAND

Department of Microtechnology and Nanosciences
Microwave Electronics Laboratory
CHALMERS UNIVERSITY OF TECHNOLOGY
Göteborg, Sweden 2013

MASTER'S THESIS IN WIRELESS, PHOTONICS AND SPACE ENGINEERING

Modeling of Power Amplifier Distortion in MIMO Transmitters

Master's Thesis in Wireless, Photonics and Space Engineering
XAVIER BLAND

Department of Microtechnology and Nanosciences
Microwave Electronics Laboratory
CHALMERS UNIVERSITY OF TECHNOLOGY
Göteborg, Sweden 2013

Modeling of Power Amplifier Distortion in MIMO Transmitters

XAVIER BLAND

©XAVIER BLAND, 2013

Master's Thesis 2013:05

ISSN 1652-8557

Department of Microtechnology and Nanosciences

Microwave Electronics Laboratory

Chalmers University of Technology

SE-412 96 Göteborg

Sweden

Telephone: + 46 (0)31-772 1000

Cover:

Simulated (left) and measured (right) distorted spectrum and spectral regrowth at the output of a MIMO transmitter for different conditions of crosstalk

Chalmers Reproservice

Göteborg, Sweden 2013

Master's Thesis in Wireless, Photonics and Space Engineering
XAVIER BLAND
Department of Microtechnology and Nanosciences
Microwave Electronics Laboratory
Chalmers University of Technology

Abstract

Facing an always growing need for higher data rate, telecommunications operators cannot rely on a bandwidth increase any more as the frequency spectrum in the UHF band is nowadays crowded. Therefore new technologies need to be developed to boost the data rate. Among those, multiple inputs multiple outputs systems (MIMO) provide both a significant rise in bit rate and a better reliability for the link. Nevertheless it is based on many antennas transmitting at the same frequency. The effect of crosstalk between antennas is prevented by ferrite isolators which introduce losses and do not fit in typical transmitter design (mostly MMIC). This thesis focuses on modeling and analysing the signal distortion due to crosstalk at the output of the power amplifier and of the MIMO transmitter in absence of isolators.

First, a static behavioural model and a dynamic model -both with dual inputs- have been developed to model the PA under conditions of crosstalk, and have been extracted for a 6W PA from CREE thanks to an active load pull measurement system. The latter model guarantees a NMSE of -32.6dB and a ACEPR of -43dB for a WCDMA signal at 2.14GHz.

Secondly, antenna arrays have been designed based on 2 microstrip patch antennas, providing different coupling between the antennas: high (-14dB), medium (-20.9dB) and low S_{12} (-28.4dB); the goal being to use the arrays for simulations and measurements.

Third, simulations of a complete MIMO transmitter were performed for a WCDMA signal at 2.12GHz and using the S-parameters of the aforementioned antenna arrays. Separating the distortion due to crosstalk from the classic non linearities of the PA, the adjacent channel leakage ratio (ACLR) is -47.3dB in case of high coupling ($S_{12} = -14\text{dB}$) and -54.3dB in case of medium coupling ($S_{12} = -20.9\text{dB}$). These values can be seen as the best achievable ACLR for a given coupling.

Finally, measurements have been performed with the same antenna arrays using a vector switched generalised memory polynomial as digital pre-distorter. The results confirm the simulations observations: the measured ACLR for the strongest coupling is -46.4dB for the WCDMA signal at 2.12GHz. Therefore the ACLR tends to increase linearly in dB with the coupling and can thus reach the -45dB limit set by 3GPP standards for a coupling around -12.4dB . The influence of crosstalk on the PA distortion is thus significant and hardly negligible in the design of MIMO transmitters for wireless communication applications.

Keywords: MIMO, crosstalk, coupling, power amplifier, modelling, memory polynomial, distortion, normalised mean square error (NMSE), adjacent channel leakage ratio (ACLR), digital pre-distorter (DPD)

Preface

This thesis project has been carried out within the GigaHertz Centre in a joint research collaboration between industrial partners and Chalmers University of Technology- at the Microwave Electronics Laboratory (MEL) and under the supervision of associate professor Christian Fager. The work is part of the energy efficient MIMO transmitters project (EMIT) led by professors Christian Fager and Thomas Eriksson.

I have been thrilled by the project and particularly by the diversity of the scientific fields the project dealt with. I am therefore delighted by this valuable experience at the GigaHertz Centre and by the new knowledge I have acquired, as well as by the global atmosphere at MEL.

From a more scientific point of view, I am pleased by the results and the new models we developed. I hope this work will be helpful for future projects in the EMIT group.

This thesis concludes my studies, both in the microwave and antenna fields at Chalmers University of Technology through the Master of Sciences Wireless, Photonics and Space Engineering, and in telecommunications at Telecom Bretagne in France. I have all along enjoyed my route, learned and experienced a lot, and I am proud of my personal route within engineering domains which delight me. I personally consider this thesis project at the GigaHertz Centre as a great reward.

Acknowledgements

This thesis work couldn't have been conducted without my supervisor Christian Fager who provided me advises, help and encouragement all along the project. I thank him a lot for the great opportunity he offered me with this project at the GigaHertz Centre.

I am also grateful to my examiner Jan Grahn, manager of the GigaHertz Centre, as well as all the colleagues of MEL for their nice attitude and their permanent smiles. The atmosphere is always relaxed and it is really stimulated to work in such atmosphere.

For their great help to define the behavioral model and for their deep implication in the measurements, I would like to express my gratitude to the EMIT members of the Signals and Systems department of Chalmers, particularly to Jessica Chani and Per Landin.

Finally, thanks to all the persons, co-workers, fellow master students and friends who provided me scientific help, entertainment and happiness!

Göteborg May 2013

Xavier Bland

Notations and abbreviations

Abbreviations

ACEPR Adjacent Channel Error Power Ratio
ACLR Adjacent Channel Leakage Ratio
ACPR Adjacent Channel Power Ratio
ADS Advanced Systems Design
CW Continuous Wave
DPD Digital Pre Distorter
DTFT Discrete-Time Fourier Transform
DUT Device Under Test
GaN HEMT Gallium Nitride High Electron Mobility Transistor
LSM Least Squares Method
LTE Long Term Evolution
MIMO Multiple Input Multiple Output
MMIC Monolithic Microwave Integrated Circuit
NMSE Normalized Mean Squared Error
PA Power Amplifier
PAE Power Added Efficiency
PCB Printed Circuit Board
PHD Polyharmonic Distortion
PSD Power Spectral Density
QAM Quadrature Amplitude Modulation
SMA SubMiniature version A
SNR Signal to Noise Ratio
WCDMA Wideband Code Division Multiple Access

Notations

A_i, B_i Incident and scattered voltage waves
 f_c, f_{res} Carrier frequency and resonance frequency
 I_{gate} Gate current
 P_{1dB} First decibel compression point (1dB compression point)
 P_{A_i} Power of the voltage wave A_i
 T Sample rate
 V_{drain} Drain voltage
 V_{gate} Gate Voltage
 x^* Conjugate of the complex number x
 Γ Reflection coefficient
 Δ Sparse time delay
 ϵ_r Relative permittivity
 $\theta_{r,q,l}, \theta_{p,q}$ Dynamic model coefficients
 λ Wavelength

Contents

Abstract	I
Preface	III
Notations	IV
Contents	V
1 Introduction	1
1.1 Background	1
1.2 Multiple Input Multiple Output Systems (MIMO)	1
1.2.1 Spatial Multiplexing Gain	2
1.2.2 Diversity Gain	3
1.3 Objectives	3
1.4 Thesis outline	3
2 Power amplifier characterisation and modeling	5
2.1 PA basics	5
2.1.1 Gain and Gain Compression	5
2.1.2 Efficiency and Power Added Efficiency (PAE)	5
2.2 Device Under Test Analysis	5
2.2.1 PA device description	5
2.2.2 Frequency	6
2.2.3 Choice of gate voltage	6
2.2.4 Power amplifier characteristics summary	6
2.3 Static Nonlinear Model: Polyharmonic Distortion Modeling	7
2.3.1 S-Parameter limitations	8
2.3.2 Polyharmonic Distortion Modeling:Black Box model	8
2.3.3 Assumptions in our case	8
2.3.4 PHD model principles	8
2.3.5 Extraction technique: Single tone active load pull measurement	10
2.3.6 Extracted scattering functions	10
2.4 Dynamic non-linear model	13
2.4.1 Memory polynomial models for power amplifiers	13
2.4.2 Double input memory polynomial model	13
2.4.3 Coefficients extraction	14
2.4.4 Coefficients selection and accuracy of the model	16
2.4.5 Accuracy comparison between the static and dynamic models	18
2.5 Linearisation of the PA	19
2.5.1 Digital Pre Distorter for the PHD model	19
2.5.2 Digital Pre Distorter for the dynamic model	20
2.6 Chapter summary	21
3 Antenna Design and Measurements	23
3.1 Microstrip antenna theory	23
3.1.1 Patch antenna design	23
3.1.2 Input impedance and inset feed	24
3.2 Antenna layout and manufacturing requirements	25
3.3 Antenna measurements	28
4 Crosstalk distortion analysis	31
4.1 Notations	31
4.2 Ideal coupling and simple MIMO model	31
4.2.1 Ideal coupling	31
4.2.2 Time delay MIMO model	31
4.2.3 Distortion analysis and ACLR	32

4.3	MIMO model with antennas	33
4.3.1	MIMO model and equations	33
4.3.2	Crosstalk distortion	35
4.3.3	Comparison with ideal coupling	40
4.4	Distortion of the radiated field	41
5	Experimental results	43
5.1	Measurement set up	43
5.2	Measurement results	44
6	Conclusions	47
6.1	Results from present work	47
6.2	Future work	47
	References	49
A	Useful definitions	53
A.1	2-port network, reflection coefficient	53
A.2	Reflected and incident voltage waves	53
A.3	IQ Data	53
A.4	Notations in this thesis	54
A.5	Mathematical tools and functions	54
A.5.1	Least Squares Method	54
A.5.2	Mean Squared Error (NMSE)	54
A.5.3	Channel Leakage Ratio	55
B	Dynamic non linear model matrices equation	57
C	Antenna Layout and Radiation Fields	58
C.1	Antenna layout in ADS	58
C.2	Radiation Fields	60
D	Measurement Set Up	61

1 Introduction

1.1 Background

Smart phones and Internet connected devices have led telecommunications operators to provide higher data rate downlink and uplink in their systems. As LTE and 4G are being developed through whole Europe, the needed capacity of telecom links gets higher and higher. In order to increase the capacity of links and the data rate, obtaining more bandwidth is crucial, and spectrum bandwidth has become a valuable and expensive raw material. Nevertheless public organizations responsible for bandwidth control cannot allow operators to increase indefinitely the bandwidth, used for other applications (maritime and aeronautical control, military frequencies). Thus telecommunications operators need to find ways and new techniques to boost the data rate without rising up the bandwidth.

MIMO (Multiple Input Multiple Output) systems are part of these technologies, enhancing both data rate and link reliability. MIMO systems are composed of at least 2 transmitting and 2 receiving antennas. They provide a considerable improvement in the data rate of the links and they reduce link failure probability thanks to spatial filtering and spatial diversity. They are nowadays widely developed and used in many different telecommunications and radar systems.

The antennas of a MIMO transmitter are emitting at the same frequency. Thus the coupling between antennas can result in a crosstalk effect: some of the signal transmitted by one antenna can be received by another transmitted antenna and so it can affect the signal emitted by this antenna. In most MIMOs, a circulator or isolator is placed between the antenna and the last power amplifier of the transmitter in order to prevent this effect, as in figure 1.1. Although this circulator is very efficient, it introduces losses and cannot be integrated in MMIC design commonly used for MIMOs. Removing these circulators can be therefore a significant improvement, but it will result in a possible crosstalk effect which would affect the behavior of the power amplifier and may introduce significant nonlinearities [6]. Indeed the coupling between two microstrip antennas can reach -11.5dB under certain conditions [12]. The aim of this study is thus to model and calculate the distortion of the power amplifier in MIMO transmitters under the crosstalk effect and without circulator.

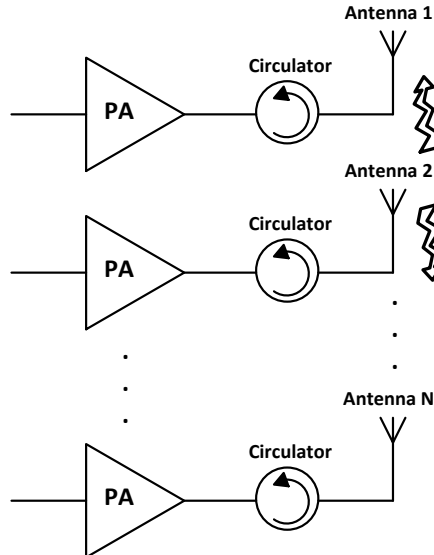


Figure 1.1: Structure of a MIMO transmitter with N antennas, including circulators

1.2 Multiple Input Multiple Output Systems (MIMO)

While most of the telecommunications links present only one input and only one output (called point to point transmission links), MIMO systems present the characteristics of having many inputs and many outputs. Considering a MIMO with M transmitters (TX) and N receivers (RX), it has no longer a vector channel but a matrix channel.

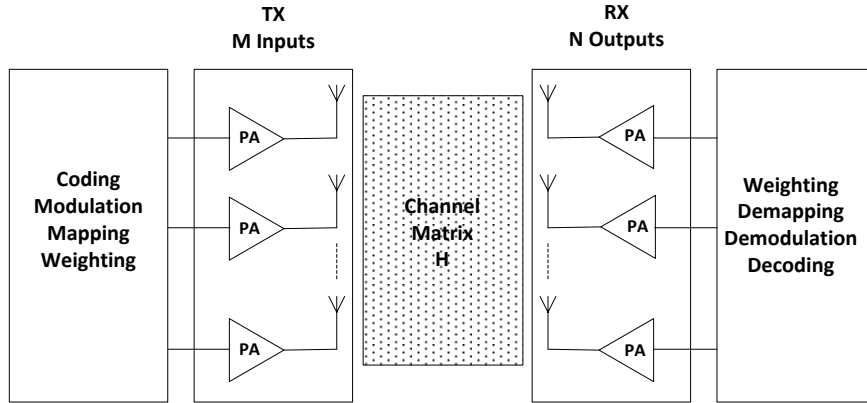


Figure 1.2: Structure and Channel Matrix of a MxN MIMO

Combining on one hand the transmitters signals and on the other hand the signals received by the receiving antennas, it is possible to enhance the bit rate and the reliability of the link [5]. Such an enhancement results in a better quality of service (QoS) and a higher data rate for the user of the telecommunication link which is crucial for the company in charge of the transmission link.

MIMOs are relying on two major principles to boost the bit rate and improve the reliability of the link: spatial multiplexing gain and diversity gain.

1.2.1 Spatial Multiplexing Gain

Without any additional bandwidth, spatial multiplexing gain allows the link using N Transmitters and N Receivers to ideally multiply the capacity of the link by N [7] [5]. The data stream is thus separated in N different parts sent to the N different TX antennas. If the scattering environment is rich enough, it is possible for the N receivers to determine the different streams using different spatial signatures for each antenna. Thus the capacity of the link can be greatly increased. This is the main advantage of MIMOs.

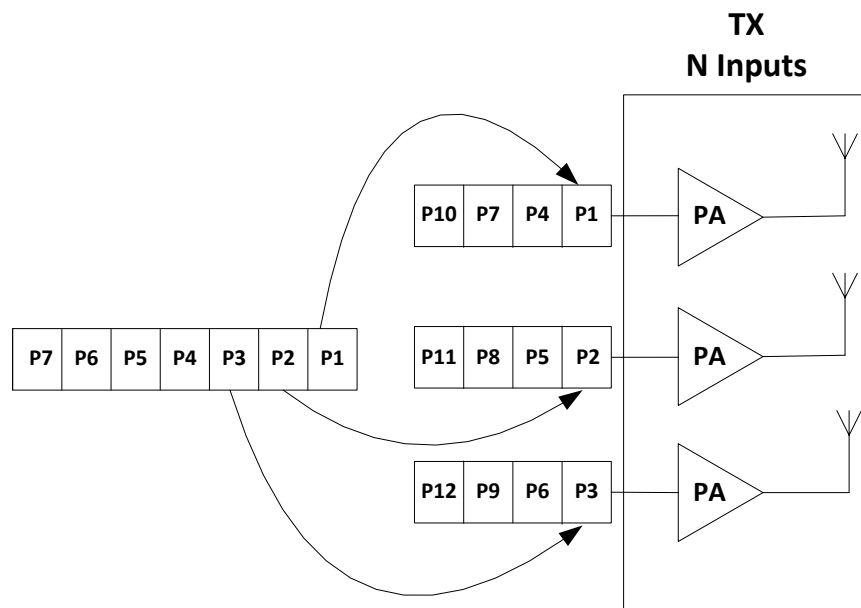


Figure 1.3: Spatial Multiplexing Gain in a MIMO

1.2.2 Diversity Gain

Whereas spatial Multiplexing is a way to increase the bandwidth, diversity is a way to increase the reliability of the link. By implementing different paths (from a fading point of view, in time, space and frequency dimensions) diversity reduces co-channel interferences and increases the signal to noise ratio (SNR) of the link [7]. The most commonly used type of diversity is spatial diversity which corresponds to antenna diversity, i.e. some spacing between the antennas. It is easy to implement as it just need more hardware, but no more bandwidth is needed and the transmission time is unchanged. Frequency and Time coding are also used for diversity gain.

1.3 Objectives

The main objective of this project is to model and analyse the distortion due to crosstalk in MIMO transmitters. Modeling the behavior of the PA is a necessary step towards MIMO simulations, particularly when measurements are not possible due to the significant size of the transmitters for $N \times N$ MIMO. As the crosstalk acts as an input for the PA, not only the ordinary input but also the crosstalk must be accounted as a secondary input for the PA. However, most behavioral models for PA are single-input models. Therefore the project aims to develop new dual-input models for PA, particularly a new dual-input dynamic model. The latter model will be extracted for a defined PA used during the entire project.

The newly developed dual-input model will be used in MIMO transmitter simulations to observe the effect of crosstalk on signal distortion. To achieve a more complete analysis, different coupling factors and coupling values shall be used.

Finally it is planned to design simple antenna arrays providing various coupling between antennas in order to perform measurements for simple MIMO transmitters. The aim of these measurements is to corroborate the results about signal distortion obtained during simulations.

1.4 Thesis outline

In this thesis we will first present a few PA basics and the characteristics of the PA used during the project, followed by the presentation of two dual-input models, first a static and then a dynamic model, which are both extracted for the considered PA.

Thereafter different two elements antenna arrays are designed, manufactured and measured to provide different coupling values. These antenna arrays, based on micro-strip antennas, are used in the project first to obtain accurate S-parameter of the array and later for measurements.

Once the S-parameter of the antenna arrays obtained, MIMO transmitters can be modeled to observe via simulation the signal distortion due to crosstalk. After first considering an ideal coupling, a complete MIMO model is set up to proceed to analysis of the signal distortion, using the dynamic model for the PA developed before.

Finally measurements are performed to obtain experimental results for the signal distortion due to crosstalk, using the different antenna arrays for various coupling values. These results are compared to the simulation results for a better analysis of the contribution of crosstalk to signal distortion.

2 Power amplifier characterisation and modeling

This chapter is divided in five distinct parts. First, PA basics are explained as well as the characteristics of the PA which is used in this project. This first part is significant as it introduces different characteristics of power amplifiers which are used throughout the whole thesis. Secondly a static behavioral model with dual-input is developed and extracted, based on polyharmonic distortion modeling [8]. Because of this static model limitations, a new dynamic dual-input model is created and extracted, based on the same principles as the previous static model. The main goal of this model is to simulate the output of the PA for modulated signals as input signals. The accuracy of both static and dynamic models is presented in the fourth part. Finally some principles for PA linearisation and for the creation of digital pre distorters are presented, considering the significant role of transmitter linearity.

2.1 PA basics

Power amplifiers are major devices in the transmitter design. It is a crucial component as it is in charge of amplifying the signal of the communication link in order to be delivered with enough power to be detected by the receiver. The amplifier must amplify the signal without creating too much noise and it should avoid amplifying the signals outside the desired bandwidth. Another crucial consideration in PA design is the amplifier power consumption: the PA is the most power demanding device of the transmission link and the more the signal will be amplified the more power the PA will consume. In this section a few properties of PAs will be presented.

2.1.1 Gain and Gain Compression

The gain of the power amplifier is defined by the ratio between the output power and the input power. As it is usually the case in the telecommunications field, it is expressed in decibels.

$$Gain = \frac{P_{out}}{P_{in}} \quad (2.1)$$

The gain is dependent on many factors linked to the properties of the amplifier and the properties of the different transistors which are used in the amplifier. The power amplifier being a nonlinear device, the gain is not constant and depends on the device, the input power, the frequency and other input parameters. Nevertheless the gain is often represented as constant, because the gain can be considered as constant over a certain bandwidth and input power range, usually small signal.

The gain compression is the reduction of the previously described slope: this is the point where the gain is not constant anymore and when the power amplifier behaves as a nonlinear device. The first dB compression point P_{1dB} is often used to describe this compression, as it represents the input power for which the real PA gain is 1dB lower than the theoretical linear slope of constant gain.

2.1.2 Efficiency and Power Added Efficiency (PAE)

The efficiency of the power amplifier can be described as the ratio of the RF output power and the power DC consumption.

$$\eta = \frac{P_{RFout}}{P_{DC}} \quad (2.2)$$

Nevertheless it is more common to express the efficiency of the PA in term of power added efficiency (PAE), which is the difference of power between the output and the input signals versus the DC consumption. It represents the efficiency of the DC current and voltage in terms of gain.

$$PAE = \frac{P_{RFout} - P_{in}}{P_{DC}} \quad (2.3)$$

2.2 Device Under Test Analysis

2.2.1 PA device description

The Device Under Test (DUT) used for this project will be the CGH40006P transistor from CREE along with the test board CGH40006P-TB. The transistor is a GaN HEMT providing a maximum

of 6W. While in the test board, the transistor behaves as an amplifier providing an average 10dB gain. The choice of such a device can be explained by the will to test new devices like GaN amplifiers which are aimed to be used in MIMO links. A simple measurement set-up using a sinusoidal RF signal source and a power meter was realized to check and confirm the performances and characteristics of the device.

2.2.2 Frequency

The frequency used is 2.14GHz. As future and actual LTE has numerous channels around 2.14GHz, it seems reasonable and useful to test the DUT at 2.14GHz. MIMO are indeed widely used in high speed data rate and in LTE networks, which explains the choice of this frequency. Nevertheless, the PA can be considered as wideband and a small change in frequency won't affect the overall performance of the PA.

2.2.3 Choice of gate voltage

The choice of the gate voltage is significant because of its influence on the gain while increasing the input power. A PA being a non-linear device particularly with high input power, it is necessary to avoid the typical PA non-linearities in order to observe the distortion due to crosstalk. Thus it is needed to determine a gate voltage and a range of input power where the gain of the PA is the most stable possible under normal conditions of excitation.

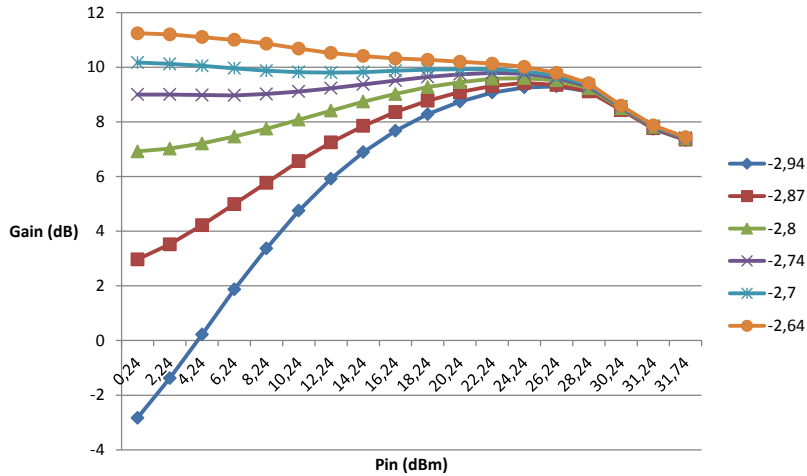


Figure 2.1: Gain compression of the PA for various gate voltages

As the figure 2.1 shows, the gain compression is very significant for large signal input power. Nevertheless a PA used in wireless communications is aimed to be driven at the maximum PAE, which is most of the time close to the gain compression point. That is why the interesting range of input power lies within intermediate and large input signals. For our PA, a good range is between 0dBm and 30dBm input power.

Using the same measurement system with the power meter and varying the gate voltage, it is possible to determine the best achievable gate voltage for which the gain of our PA is the most constant over the desired range of input power. According to figure 2.2, this gate voltage is about $V_{gate} = -2.71V$.

2.2.4 Power amplifier characteristics summary

To test the device and to check its characteristics, we used the same measurement system described above. The values for the different parameters are shown below:

$$V_{Gate} = -2.71V$$

$$I_{Drain} = 0.69A$$

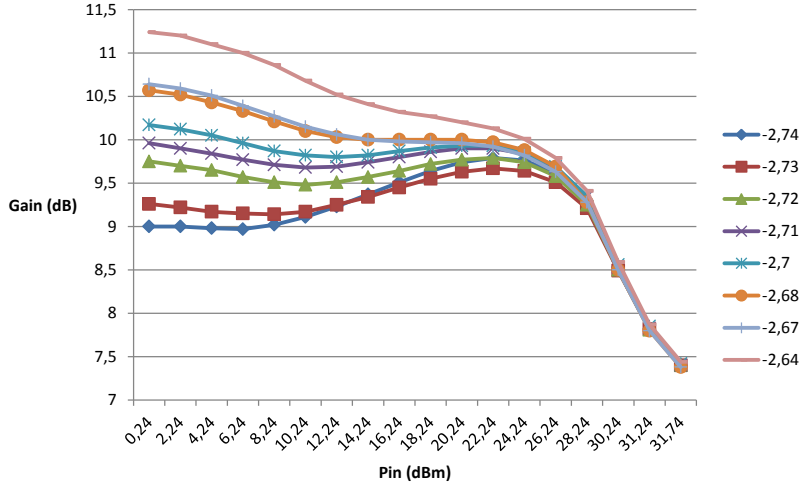


Figure 2.2: Detailed gain compression for various gate voltages

$$V_{Drain} = 28V$$

In figure 2.3 the gain and the PAE of the device are shown. We can calculate by interpolation that the 1-dB compression point is about $P_{in} = 29.5\text{dBm}$ and that the maximum PAE is about 54.2% around $P_{in} = 30.2\text{dBm}$.

$$P_{1dB} = 38.3\text{dBm} @ 29.5\text{dBm}$$

$$PAE_{max} = 54.2\% @ P_{in} = 30.2\text{dBm}$$

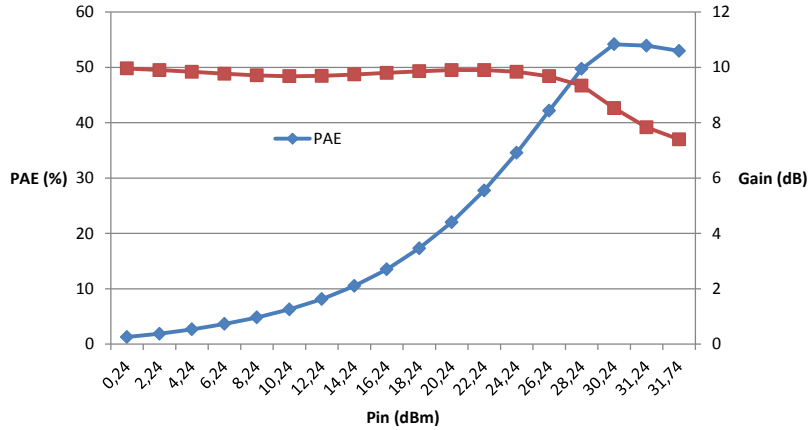


Figure 2.3: PAE and gain of the device at -2.71V voltage at the gate

As we can see in figure 2.3, the gain is definitely not constant even if the input power is limited to 26dBm. Moreover the PA is characterised without taking the crosstalk into account. To observe the PA response under conditions of crosstalk it is necessary to develop a dual input behavioral model.

2.3 Static Nonlinear Model: Polyharmonic Distortion Modeling

Behavioral models are useful for simulating and observing the output of the PA for various modulated signals without performing measurements, which can be difficult to set up. Nowadays most of the behavioral models are single-input models and are thus unable to take crosstalk into consideration. Therefore dual-input models are developed to observe the signal distortion due to crosstalk, starting with a static dual-input model. This model is based on the model developed by Jan Verspecht and David Root called the Polyharmonic Distortion Modeling (PHD model) [8].

2.3.1 S-Parameter limitations

As described in appendix A.1 the S-parameters are very useful to describe linear behavior. However, as it was clearly observed in the previous section, power amplifiers are nonlinear devices, and even though S parameters can give a good approximation of the trend of the behavior of such devices, it is definitely limited when it comes to estimating precisely the nonlinear behavior of power amplifiers, particularly under large signal conditions. New models have thus to be set up to model this nonlinear behavior.

2.3.2 Polyharmonic Distortion Modeling:Black Box model

The PHD model can be seen as a black box frequency-domain modeling technique [8]. It means that no knowledge concerning how the DUT is realised is necessary to establish the model for the DUT and to extract the coefficients of this model. Thus this black box approach is technology independent and can be fitted to any other amplifier different from the one we are testing. The coefficients composing the model are extracted by looking at the output voltage wave B_2 of the amplifier as function of the input voltage waves A_1 and A_2 (the measurements performed for the extraction are presented in section 2.3.5). However a black box approach has one major constraint: the extracted model will be adapted only to signals close to the ones used to stimulate the DUT. That means that a wide range of input signals are necessary to extract the coefficients of the model if a the extracted model is meant to be not too specific.

2.3.3 Assumptions in our case

The PHD model is a frequency domain modeling technique, which implies that many harmonics are present both at the input and at the output. As described in the introduction crosstalk effects in MIMO occur because of frequency re-use, i.e. the use of the same frequency in the different antennas of a MIMO transmitter. Thus we are mainly interested in the effect at this frequency. Moreover many filters are used in a transmitter for wireless communications which implies that all harmonics except the fundamental are filtered out at the output of the PA. That's why we will consider for now only the fundamental harmonic terms in the PHD model.

2.3.4 PHD model principles

As it is explained in [8], the PHD model is based on the same principle as the S parameters and can be considered as a large signal extension of the S parameters. It is based on the travelling voltage waves A (the incident waves) and B (the scattered waves) described in appendix A.1.

Considering a general N-port network, the output of an amplifier can be expressed as a nonlinear function F_{pm} of the incident traveling voltage waves [8]:

$$B_{pm} = F_{pm}(A_{11}, A_{12}, \dots, A_{21}, A_{22}, \dots) \quad (2.4)$$

where p in B_{pm} and A_{pm} expresses the number of the concerned port and m is the number of the concerned harmonic, the index 1 being the fundamental harmonic. If we reconsider this equation for a two port network and assuming the limitation about the neglected harmonics, we have

$$B_{21} = F_{21}(A_{11}, A_{21}) \quad (2.5)$$

To simplify this part and because only the fundamental frequency is considered, B_{21} , A_{11} and A_{21} will be from here onwards abbreviated as B_2 , A_1 and A_2 , respectively.

An important property of the PHD model is that the non-linear function F_{21} is time invariant. Indeed the system is considered as static. Applying a time delay to the input waves A_{pm} results in the same time delay for the output signals, and in the frequency domain it corresponds to a linear phase shift:

$$\cos(\omega(t + \Delta t)) \xrightarrow{\text{Frequency domain}} e^{j\omega(t+\delta t)} = e^{j\omega t} e^{j\theta} \quad (2.6)$$

and then

$$B_2 e^{j\theta} = F_{21}(A_1 e^{j\theta}, A_2 e^{j\theta}) \quad (2.7)$$

If we set this phase shift to the opposite phase of A_1 , $\phi(A_1)$, and if we define $P = e^{j\phi(A_1)}$, we have:

$$B_2 P^{-1} = F_{21}(|A_1|, A_2 P^{-1}) \quad (2.8)$$

Because the effect of crosstalk is small compared to the non linearities of the PA, the effect of the wave A_1 is considered as dominant and the effect of A_2 small relative to A_1 . It is thus possible to use the properties of small signal modeling [8] and apply these properties in (2.8):

$$F_{21}(|A_1|, A_2 P^{-1}) = F_{21}(|A_1|, 0) + \Delta(A_2 P^{-1}) \quad (2.9)$$

As $\Delta(A_2 P^{-1})$ is small relative to A_1 , the linear response in $A_2 P^{-1}$ can be computed as a derivative:

$$\Delta(A_2 P^{-1}) = F(A_1, A_2 P^{-1}) - F(A_1, 0) = \left. \frac{\partial F(A_1, A_2 P^{-1})}{\partial A_2 P^{-1}} \right|_{(A_1, 0)} A_2 P^{-1} \quad (2.10)$$

Separating the real and imaginary parts of $A_2 P^{-1}$ to proceed the derivation, B_2 can be expressed as [8]:

$$B_2 = K_{21}(|A_1|) P^{+1} + G_{22}(|A_1|) P^{+1} \Re(A_2 P^{-1}) + H_{22}(|A_1|) P^{+1} \Im(A_2 P^{-1}) \quad (2.11)$$

with

$$K_{21}(|A_1|) = F_{21}(|A_1|, 0)$$

$$G_{22}(|A_1|) = \left. \frac{\partial F_{21}(|A_1|, A_2 P^{-1})}{\partial \Re(A_2 P^{-1})} \right|_{(|A_1|, 0)}$$

and

$$H_{22}(|A_1|) = \left. \frac{\partial F_{21}(|A_1|, A_2 P^{-1})}{\partial \Im(A_2 P^{-1})} \right|_{(|A_1|, 0)}$$

Replacing $\Re(z)$ and $\Im(z)$ par $\frac{z + z^*}{2}$ and $\frac{z - z^*}{2j}$ we obtain [8]:

$$B_2 = K_{21}(|A_1|) P^{+1} + G_{22}(|A_1|) P^{+1} \left(\frac{A_2 P^{-1} + \text{conj}(A_2 P^{-1})}{2} \right) + H_{22}(|A_1|) P^{+1} \left(\frac{A_2 P^{-1} - \text{conj}(A_2 P^{-1})}{2j} \right) \quad (2.12)$$

So, formulated in another way [8]:

$$B_2 = S_{21}(|A_1|) A_1 + S_{22}(|A_1|) A_2 + T_{22}(|A_1|) P^2 A_2^* \quad (2.13)$$

where

$$S_{21} = \frac{K_{21}(|A_1|)}{|A_1|}$$

$$S_{22} = \frac{G_{22}(|A_1|) - jH_{22}(|A_1|)}{2}$$

and

$$T_{22} = \frac{G_{22}(|A_1|) + jH_{22}(|A_1|)}{2}$$

are the scattering coefficients of the PHD model.

In the equation above we can observe that the scattering coefficients S_{21} and S_{22} are very close to the S parameters. Moreover, if A_2 is set to zero, S_{21} is exactly the S parameter giving the relation between B_2 and A_1 . This scattering coefficient is very useful to check whether the extracted model is consistent or not.

A major difference between classic S parameters and the PHD model defined in (2.13) is the presence of the conjugate of A_2 . If we consider only the influence of A_2 on B_2 , which can be considered partly as a possible consequence of the crosstalk effect:

$$\frac{\Delta B_2}{A_2} = S_{22}(|A_1|) + T_{22}(|A_1|) P^2 Q^2 = S_{22}(|A_1|) + T_{22}(|A_1|) e^{2j(\phi_{A_1} - \phi_{A_2})} \quad (2.14)$$

The influence of A_2 on B_2 depends thus not only on the amplitude of A_1 but also on the phase difference between A_2 and A_1 . The three scattering functions S_{21} , S_{22} and T_{22} must then be extracted from measurements with different amplitude values of A_1 , different amplitude values of A_2 and different phase difference between A_1 and A_2 .

2.3.5 Extraction technique: Single tone active load pull measurement

As aforementioned the scattering coefficients of the PHD model need to be extracted with real measurements and will fit a particular device (in our project the CREE transistor CGH40006P in its test board CGH40006P-TB). To extract the different coefficients a range of various amplitude and phase for A_1 and A_2 are needed. That means that we have to inject different A_1 and A_2 incident waves into the DUT and measure the resulting A_1 , A_2 and B_2 waves, both amplitude and phase.

An active load pull measurement system seems fitted for this purpose, as it is possible to control the amplitude and phase of the incident waves that are injected. In the same time it is possible to calculate the reflection coefficient of the load as function of B_2 and A_2 , $\Gamma_L = \frac{A_2}{B_2}$, as seen in figure 2.4. Moreover it is possible to program the measurement for many ranges of amplitude and phase for the different incident waves, and measure in a very short time.

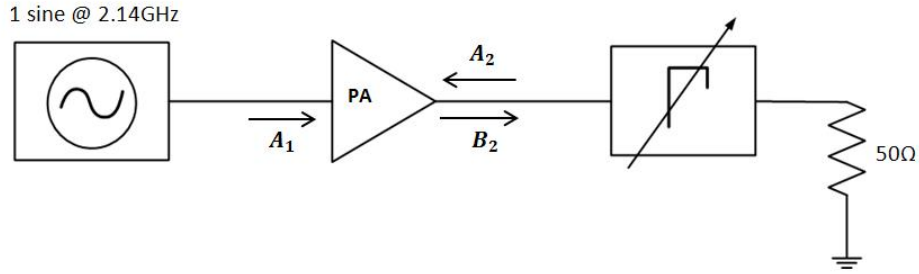


Figure 2.4: Single tone load-pull system used to extract the output B_2 for various amplitude and phase of the input signals A_1 and A_2

An active load pull measurement system has been developed [9] within the GigaHertz Centre at Chalmers University of Technology. This is the one we will use for our measurement and coefficient extractions.

The main principle of the active load pull is to send a single tone incident wave A_1 along with a single tone wave A_2 in the DUT instead of varying the output impedance like in a classic load pull measurement [9]. This active principle enables us to have a better control on the incident waves, particularly for A_2 , and thus better measurements.

The measurement itself consists of two steps. First the amplitude of A_1 is fixed, but the amplitude $|A_2|$ will be varying in order to match the reflection coefficient at the load Γ_L with 6 different fixed values Γ_i from -6dB to -20dB . The second step is to change the value of $|A_1|$ and proceed as before with $|A_2|$ to match the same values of the reflection coefficient Γ_L . The process is repeated for 9 different amplitude of $|A_1|$ to obtain different values of the scattering coefficients by using a Least Mean Squares algorithm in MATLAB. For a given magnitude of $|A_1|$, we can thus have:

$$\begin{bmatrix} B_{2,\Gamma_1} \\ B_{2,\Gamma_2} \\ \vdots \\ B_{2,\Gamma_6} \end{bmatrix} = \begin{bmatrix} A_{1,\Gamma_1} & A_{2,\Gamma_1} & A_{2,\Gamma_1}^* e^{\phi_{A_1,\Gamma_1}} \\ A_{1,\Gamma_2} & A_{2,\Gamma_2} & A_{2,\Gamma_2}^* e^{\phi_{A_1,\Gamma_2}} \\ \vdots & \vdots & \vdots \\ A_{1,\Gamma_6} & A_{2,\Gamma_6} & A_{2,\Gamma_6}^* e^{\phi_{A_1,\Gamma_6}} \end{bmatrix} \begin{bmatrix} S_{21}(|A_1|) \\ S_{22}(|A_1|) \\ T_{22}(|A_1|) \end{bmatrix} \quad (2.15)$$

which can be solved using the function backslash \ in MATLAB (see appendix A.5.1).

2.3.6 Extracted scattering functions

Values of $S_{21}(|A_1|)$, $S_{22}(|A_1|)$ and $T_{22}(|A_1|)$ have now been extracted for all values of $|A_1|$. The scattering functions, i.e. the functions S_{21} , S_{22} and T_{22} can be retrieved by fitting the extracted coef-

ficients using a *spline* or polynomial fitting function in MATLAB. The obtained scattering functions are plotted in figures 2.5, 2.7 and 2.8.

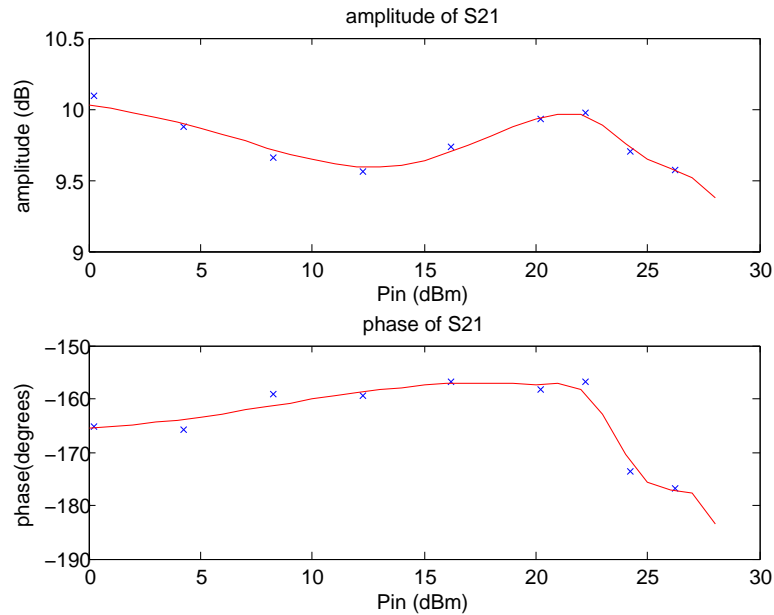


Figure 2.5: Magnitude and phase of the scattering function S_{21}

The magnitude of S_{21} behaves like the gain of the DUT. Indeed $S_{21}(|A_1|)A_1$ is the only part in (2.13) remaining if there is no reflection due to mismatch nor incident wave at the output due to crosstalk, i.e. $A_2 = 0$. It also means that the scattering function S_{21} corresponds to the S-parameter S_{21} . It is thus possible to compare the extracted scattering function S_{21} with the gain previously measured in figure 2.3. As this measurement has been done with a power meter supposed matched with the PA, we can assume that there was no reflection at the load, and so the gain can be compared to S_{21} . This comparison is plotted in figure 2.6. The two curves are close even though a few differences appear. It can be explained by either a lack of accuracy in both measurements, or by a possible mismatch at the load of the PA (also possible for both measurements).

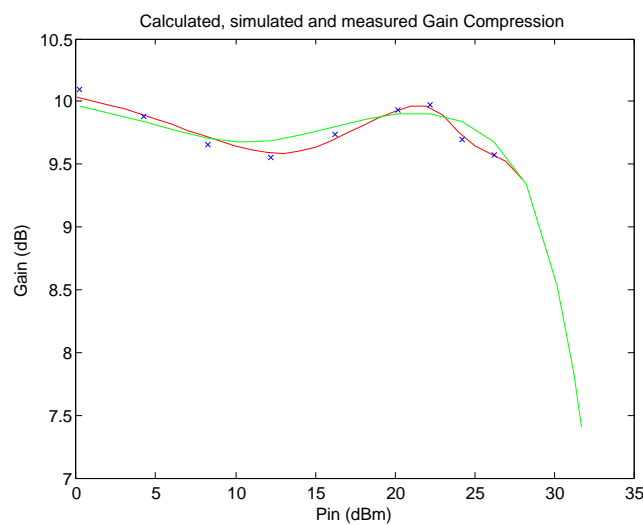


Figure 2.6: Measured Gain (green curve) and gain simulated with the static model (red curve)

The last coefficient T_{22} is typical of a large signal phenomenon: it is small enough to have no

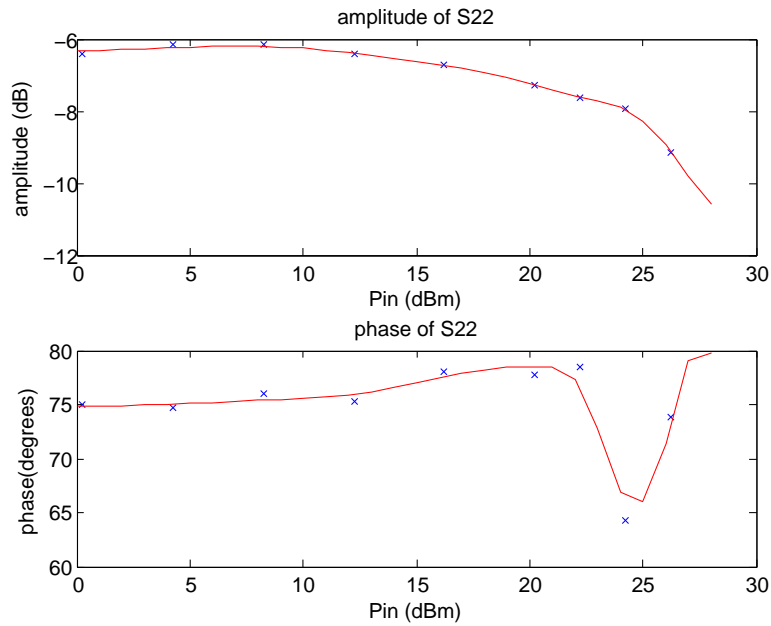


Figure 2.7: Magnitude and phase of the scattering function S_{22}

influence on the output for small signal at the input and it increases significantly for large signal at the input, clearly showing that the device behaves like a strongly non-linear device under large signal conditions.

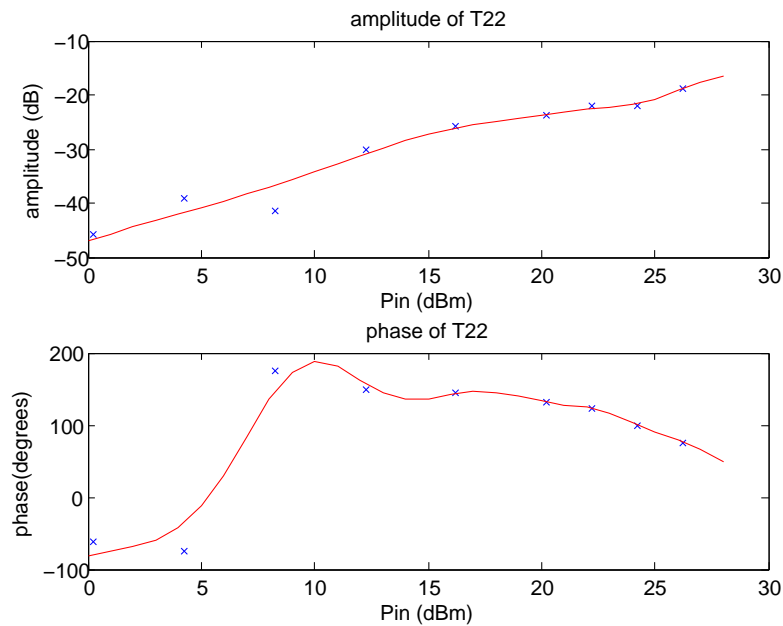


Figure 2.8: Magnitude and phase of the scattering function T_{22}

As the measurements done with the load-pull system have been done up to 26dBm input, it is not possible to simulate the output of the PA for an input power higher than 26dBm. Nevertheless it is not necessary to have an input signal with higher power than 26dBm, as the gain compression of the amplifier starts already around 26dBm. So limiting the input power to 26dBm, the non-linearities introduced by the amplifier remain small.

2.4 Dynamic non-linear model

2.4.1 Memory polynomial models for power amplifiers

The static non-linear model is frequency independent and it can accurately represent the output of the amplifier for a single frequency or a narrowband input signal. However, in most modern telecommunication systems (LTE, WCDMA and 2G) the input signals are modulated and their bandwidth is significant. Therefore the memory effects cannot be neglected and developing a new dual-input model including memory is essential. Moreover, thermodynamic effects can occur in the PA (as an example, when the PA is being heated up) and it can result in memory effects for the output of the PA. Therefore a dynamic model has been created, based on a memory polynomial.

Memory polynomial models are suitable to describe the non-linear behavior of a PA including memory effects. Considering the input and output travelling voltage waves A_1 and B_2 only, it can be expressed [4] as:

$$B_2(n) = \sum_{q=0}^Q \sum_{p=1}^P \theta_{q,p} A_1(n-q) |A_1(n-q)|^{2(p-1)} \quad (2.16)$$

where n corresponds to a time sample and q corresponds to a time delay. P is the maximum order of the polynomial in A_1 and Q is the total number of memory delays involved in the equation. $\theta_{q,p}$ are the complex coefficients of the model and can be evaluated for each PA according to a least squares method. The previous equation contains only odd-order coefficients: indeed the even-order terms result in a signal far away (in terms of frequency) from the carrier, and thus this signal will be filtered out[4]. Equation (2.16) can also be written in function of A_1 and A_1^* only:

$$B_2(n) = \sum_{q=0}^Q \sum_{p=1}^P \theta_{q,p} (A_1^*)^{p-1} (n-q) A_1^p(n-q) \quad (2.17)$$

As we can see in (2.17) the order in A_1 is one degree higher than the order in A_1^* , which is typical in memory polynomial for PA behavioral modeling: the total order of the normal terms will remain one degree higher than the total order of the conjugate terms. Other terms can be obtained by conjugating the latter. Therefore other terms are pruned to respect this statement.

Models with linear memory can either use uniform time-delay taps or non uniform time-delay. In the first case, the time-delay between each considered signal to calculate the output at the sampled time n is the same, whereas models with non uniform time-delay are using a non-uniform distribution to express the different delays. As non-uniform delays are difficult and take long time to be computed, the best choice for our model is to consider a uniform time-delay memory. To extract the coefficients of the model, time domain data has to be acquired. This implies a conversion from analogue to discrete time signal and so a sampling rate had to be defined. This time sampling rate will be the unit for our uniform time-delay. In our case, as the device used will be oversampling the data, we shall use a sparse delay technique. That means that the unit time-delay (the sparse delay) between each of the considered terms will be equal to Δ , where $\Delta = N \times T$ and T is the sample duration. The previous equation can be thus written as:

$$B_2(t) = \sum_{q=0}^Q \sum_{p=1}^P \theta_{q,p} A_1(t-q\Delta) |A_1(t-q\Delta)|^{2(p-1)} \quad (2.18)$$

and the total number of coefficients is $P(Q+1)$.

2.4.2 Double input memory polynomial model

If we want to include the effect of crosstalk in our model, we thus need to introduce a second input in our memory polynomial model (as we introduce the travelling voltage wave A_2 in the PHD model). However it is not realistic to consider that this second input A_2 would lead to the same effect as the first and main input A_1 . As the effect of crosstalk can be considered as small compared to the influence of A_1 , the function of the travelling voltage wave A_2 can be considered as linear, thanks to the small signal approximation. As a result the terms $A_2 |A_2|^{2(p-1)}$ won't be considered in the model, but cross products between A_2 and a polynomial function in A_1 will appear.

As aforementioned in the previous section, it is usual in PA behavioral modeling to keep only the terms where the total order of normal terms is one degree higher than the total order of the conjugate terms. Thus only the terms $A_2|A_1|^{2(l-1)}$ and $A_2^*A_1^2|A_1|^{2(l-2)}$ remains. These two cross products are similar to the terms forming the PHD model in (2.13), with a part in $A_2F(|A_1|)$ and another in $A_2^*G(|A_1|)e^{j\phi_{A_1}}$ where $F(|A_1|)$ and $G(|A_1|)$ are functions of $|A_1|$ and ϕ_{A_1} is the phase of A_1 . The equation of the model is then the sum of (2.18) and the term:

$$\sum_{r=0}^Q \sum_{q=0}^Q \sum_{l=1}^L \theta_{r,q,l} A_2(t-r\Delta) |A_1(t-q\Delta)|^{2*(l-1)} + \theta_{r,q,l} A_2^*(t-r\Delta) A_1^2(t-q\Delta) |A_1(t-q\Delta)|^{2*(l-2)} \quad (2.19)$$

where L is the maximum order of the polynomial model for the parts involving A_2 and A_2^* .

To sum up, here is the complete equation of our dynamic model:

$$\begin{aligned} B_2(t) = & \sum_{q=0}^Q \sum_{p=1}^P \theta_{q,p} A_1(t-q\Delta) |A_1(t-q\Delta)|^{2(p-1)} \\ & + \sum_{r=0}^Q \sum_{q=0}^Q \sum_{l=1}^L \theta_{r,q,l} A_2(t-r\Delta) |A_1(t-q\Delta)|^{2(l-1)} \\ & + \sum_{r=0}^Q \sum_{q=0}^Q \sum_{l=2}^L \theta_{r,q,l} A_2^*(t-r\Delta) A_1^2(t-q\Delta) |A_1(t-q\Delta)|^{2(l-2)} \end{aligned} \quad (2.20)$$

A significant task is now to determine the best values for the number Q , P and L , which set the degree of the polynomial model (P and L) and the number of coefficients as well as the degree of memory, i.e. the number of delays (Q) considered to calculate the output signal at the time t .

The number M of coefficients will be function of the 3 parameters L, P and Q and equal to:

$$M = LQ^2 + (P + 2L)Q + P + L \quad (2.21)$$

2.4.3 Coefficients extraction

As the created model is a dynamic model, it is not suitable to excite the PA with a CW signal as we did in section 2.3.5 to extract the coefficients for the (quasi) static PHD model. Nevertheless, we can see a time domain signal as a multi sine signal in the frequency domain, and thus it is possible to simultaneously send different sines (or frequency tones) to obtain a modulated time domain signal. Assuming K the number of frequencies from each side of the carrier frequency f_c and Δ_f the frequency spacing, the complex modulated signal can be expressed in function of the time t using a discrete-time Fourier transform (DTFT):

$$A_{1,modulated}(t) = \sum_{k=0}^{2K} F_{A_1,k} e^{j(\Phi_k + (k-N)\Delta_f \times 2\pi t)} e^{j2\pi t f_c} \quad (2.22)$$

where $F_{A_1,k}$ and Φ_k are respectively the amplitude and the phase of the k^{th} tone and t the time vector. The complex baseband signal can thus be written as:

$$A_{1,baseband}(t) = \sum_{k=0}^{2K} F_{A_1,k} e^{j(\phi_k + (k-N)\Delta_f \times 2\pi t)} \quad (2.23)$$

where the complex baseband signal $A_{1,baseband}(t)$ can be seen as IQ data (see appendix A.3).

One of the main advantage of the active load pull measurement developed within the GigaHertz Centre and explained above in section [9] is that the system is also suitable for multi-sine signal excitations: it is not only possible to generate a single tone measurement, but many frequency tones at the same time. Therefore it is possible to generate modulated signals around a certain carrier frequency f_c and retrieve the time domain signal by following the previously described steps. We will proceed in the exact same way to obtain the different signals $A_1(t)$, $A_2(t)$ and $B_2(t)$ needed to extract the coefficients of the model.

To extract the coefficients of our model for our PA, 15 tones have been considered around the carrier frequency $f_c = 2.14\text{GHz}$ separated each by a spacing $\Delta_f = 1\text{MHz}$. In this way the covered spectrum is similar to the spectrum of a WCDMA or LTE channel (5MHz bandwidth) along with the two adjacent upper and lower channels (5MHz each), for a total spectrum bandwidth of 15MHz. In our case and using 15 tones separated by $\Delta_f = 1\text{MHz}$, one can argue that the true bandwidth is thus limited to 14MHz; nevertheless the shape of the signal spectrum will be roughly the same with the same bandwidth for all main and adjacent channels. In this measurement the input spectrum A_1 is considered as a single main channel of 5MHz, and it is thus composed of only 5 tones. However, in reality the signal would have been first through a DPD and spectral regrowth in the adjacent channel could have been considered. The multi-sine active load pull measurement system and the generated frequency spectrum stimulated at the two inputs (A_1 and A_2) and the spectrum obtained at the output (B_2) are presented in figure 2.9.

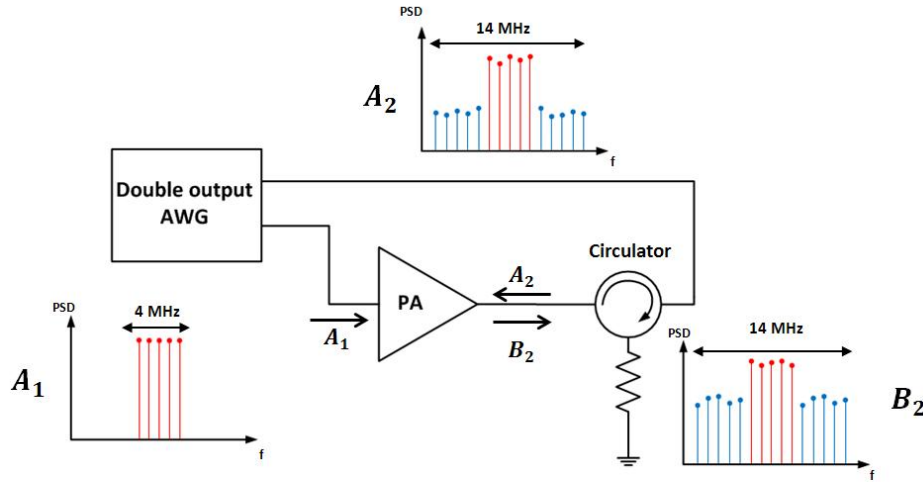


Figure 2.9: Active load-pull system and generated signals A_1 , A_2 and B_2 used to extract the coefficients of the dynamic model

To extract the coefficients different time domain signals $A_1(t)$, $A_2(t)$ and $B_2(t)$ are needed. These time domain signals can be retrieved from the frequency tones generated by the multi-sine active load pull system and using a DTFT (the method is explained above). If we consider the signal in the frequency domain, i.e. the different tones, we can describe the measurements as the following. First, the amplitude and the phase of the different tones $F_{A_1,k}$ composing A_1 are set to obtain a maximum peak value of $A_1(t)$ between 18dBm and 26dBm. Then the amplitude and phase of the different tones $F_{A_2,k}$ composing A_2 are chosen to obtain coupling values between $B_2(t)$ and $A_2(t)$ from -20dB to -6dB (6 different coupling values in total). It is significant to notice that the phase of the tones $F_{A_2,k}$ have been taken randomly to obtain a greater diversity in the measured data. Once the tones $F_{B_2,k}$ measured at the output of the PA to form $B_2(t)$, the whole process is repeated for different amplitudes of the tones $F_{A_1,k}$ in order to switch the maximum peak value of $A_1(t)$. Thus, 5 maximum peak values of $A_1(t)$ are processed.

For each set of tones $F_{A_1,k}$, $F_{A_2,k}$ and $F_{B_2,k}$, the time domain baseband signals $A_1(t)$, $A_2(t)$ and $B_2(t)$ are retrieved. The coefficients of the dynamic model can now be extracted thanks to a LSM algorithm in MATLAB, using the oversampling rate T of the oscilloscope to obtain bigger matrices and a better accuracy. The sparse delay used in the dynamic model is set approximately to the sample delay of a WCDMA signal, i.e. $\Delta = \frac{1}{\Delta_{f_s, \text{WCDMA}}} = \frac{1}{30.72\text{MHz}} = 32.6\text{ms}$.

Finally, the equation to extract the coefficients can be presented as:

$$\mathbf{B}_2 = \mathbf{H}(A_1, A_2)\boldsymbol{\theta} \quad (2.24)$$

where these matrices are described in appendix B.

Once the coefficients extracted, it is now important to analyse the accuracy of this new model and determine if it is accurate enough to simulate output signals close enough to real (measured) output signals, given the same input signals.

2.4.4 Coefficients selection and accuracy of the model

The accuracy of the model is linked to the choice of the number of coefficients, that means that we should select the numbers P , Q and L to obtain a good compromise between good accuracy of the model and a coherent and realistic calculation time (linked to the complexity of the model). Indeed, the more coefficients there are, the more complex the model becomes: the time to extract the coefficients and to calculate the output of the simulated PA grows exponentially with the parameter Q , and linearly with P and L . To obtain an accurate enough model we calculated the NMSE between the simulated output of the PA and the real output signal for the same input. To be more realistic, the coefficients have been extracted with signals which are different from the input signals used to calculate the NMSE. The extraction has been realised with a bunch of A_1 , A_2 and B_2 from the measurements realised before in section 2.4.3 and for an input power of maximum 24dBm and 26dBm. Indeed the accuracy of the model relies also on the data used for the extraction of the coefficients.

Both the coefficients extractions and the calculations for the NMSE have been carried for different values of P , L and Q . Comparing the NMSE, we can choose reasonable values for these three parameters. The NMSE is also related to the noise in the measurements: indeed some small variations are due to the noise and it is useless for us to model it. That is why we will calculate the NMSE with signals different from the ones used to extract the coefficients. Moreover, it is important to consider that too much coefficients can also fit the noise instead of the signal, in addition to increasing complexity of the model. So we will limit ourself in the number of involved coefficients.

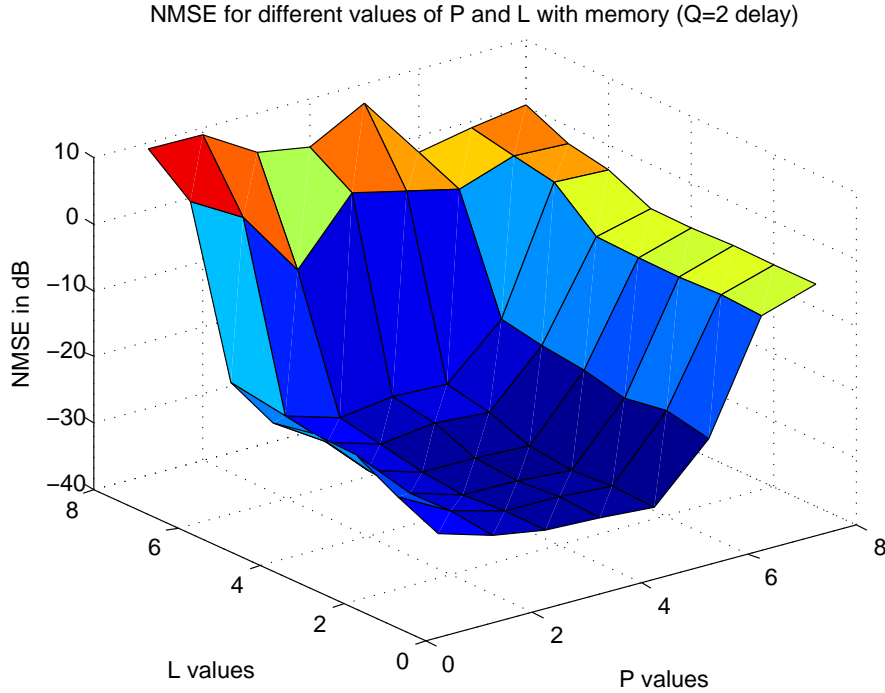


Figure 2.10: NMSE in dB for the dynamic model, with $Q = 2$ and coefficients calculated with input signals of 24dBm and 26dBm maximum input power

In figure 2.10 NMSE as function of the value of P , L and Q is shown. We can observe in figure 2.10 that $2 \leq P \leq 6$ and $1 \leq L \leq 4$ for a value of $Q = 2$ guarantee an NMSE below -30 dB.

To be a bit more accurate, the figures 2.11 and 2.12 shows that the NMSE is improved for higher values of P than the value of L , which confirms that the coupling effect stay small relative to the main non linearity of the PA. This assumption was also made in the PHD model definition when saying the crosstalk effect was a small signal effect. Nevertheless a value of P higher than $P = 5$ result in a fast decrease of the NMSE as we can see in figure 2.11. A good compromise would be to choose the parameters P and L for the dynamic model as $P = 4$ and $Q = 2$, for both a good accuracy of the model and a limited complexity of $2Q^2 + 8Q + 4$ coefficients, so 28 coefficients for

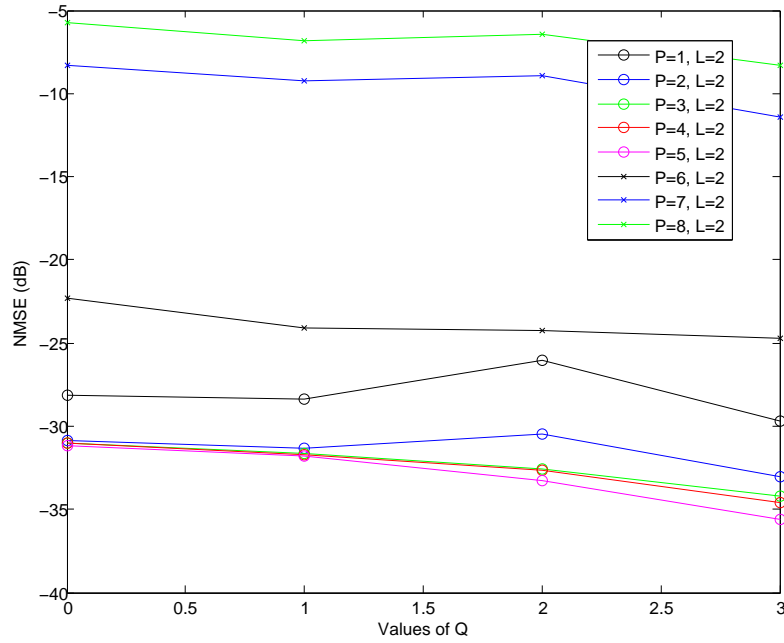


Figure 2.11: NMSE in dB for the dynamic model in functions of the degree P and the number of considered delays Q , with fixed $L = 2$

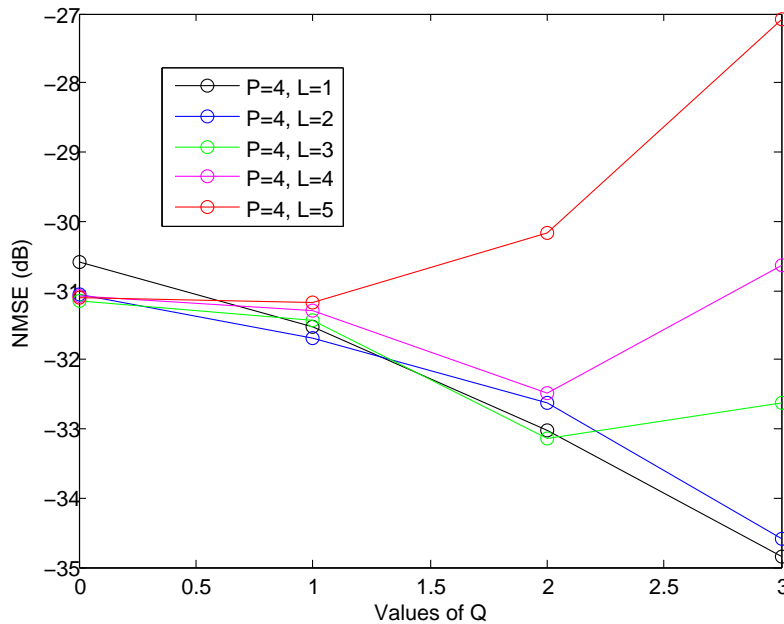


Figure 2.12: NMSE in dB for the dynamic model in functions of the degree L and the number of considered delays Q , with fixed $P = 4$

$Q = 2$. Concerning the memory parameter Q , it seems that the more delays are considered, the more improved is the NMSE. However this statement for certain values of the parameters (P, L) is not true for $Q > 2$ (see figure 2.12). The value $Q = 2$ is also a good compromise between good accuracy for the model and its complexity (only 28 coefficients with $P = 4$ and $L = 2$). For now on, the parameters P, L and Q for the dynamic model are set to $P = 4, L = 2$ and $Q = 2$, which guarantee a NMSE of -32.6 dB. This NMSE value is very close to other reference models like the modified Saleh polar model ($NMSE = -32$ dB [4]), complex power series at the 13th order ($NMSE = -33.4$ dB [4]) or the Bessel Fourier model with seven terms ($NMSE = -33.5$ dB [4]), and yet the developed dynamic model considers the second incident wave A_2 and can therefore model mismatch and crosstalk effects, which is not possible for any of the others. The model can thus be seen as a complex power series at the 9th order for A_1 (as stated in 2.18) and at the 4th order for A_2 (as stated in 2.19), and including memory consideration with 2 delays.

The average ACEPR for the model calculated over all the measurements is $ACEPR = -43$ dB (see figure 2.13). One can see in this figure that the ACEPR suffers more variations for higher peak power of the multi-sine signal A_1 . This is mainly due to less accuracy for the measurement.

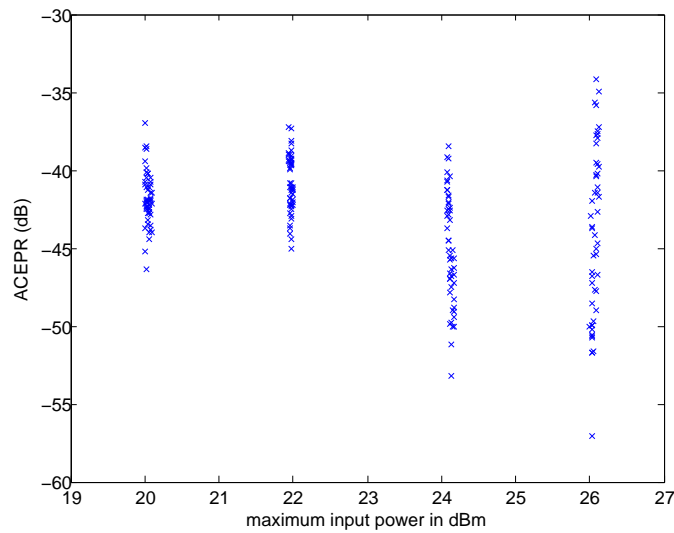


Figure 2.13: ACEPR in function of the maximum peak power of the multi-sine input signal A_1 . Calculated over all the measurements with $P = 4, L = 2$ and $Q = 2$.

2.4.5 Accuracy comparison between the static and dynamic models

To compare the accuracy of this dynamic model with the accuracy of the previously introduced static model, we used the data provided by the measurements performed for the dynamic model. This data is obviously independent from the data used to extract the scattering coefficients and the scattering functions of the static model. Concerning the scattering functions, they have been extracted using a *spline* method in MATLAB. Because of their specificity due to the *spline* method to pass through each point used for the extraction, they are more accurate than polynomial functions. Therefore this *spline* extraction method results in the best achievable NMSE when it comes to obtain the accuracy of the model. In figure 2.14 is presented the NMSE for the static model, comparing the output simulated for the input signals used to extract the coefficients of the dynamic model, and the data measured as output of the PA during the measurement performed for the dynamic model. To obtain this figure, all the data used for the dynamic model extraction has been used. All the data is plotted, starting on the left with the data provided by the measurement with the highest maximum peak power of the main input signal, and finishing on the right with the measurement with the lowest maximum peak power of the main input signal.

The worst NMSE obtained is -9 dB, and the average NMSE is thus around -10 dB. This result is obviously not good when comparing to the NMSE obtained for the dynamic model (as seen in section 2.4.4, $NMSE_{dynamic} = -32.6$ dB, so an improved NMSE by more than 20dB), which means that

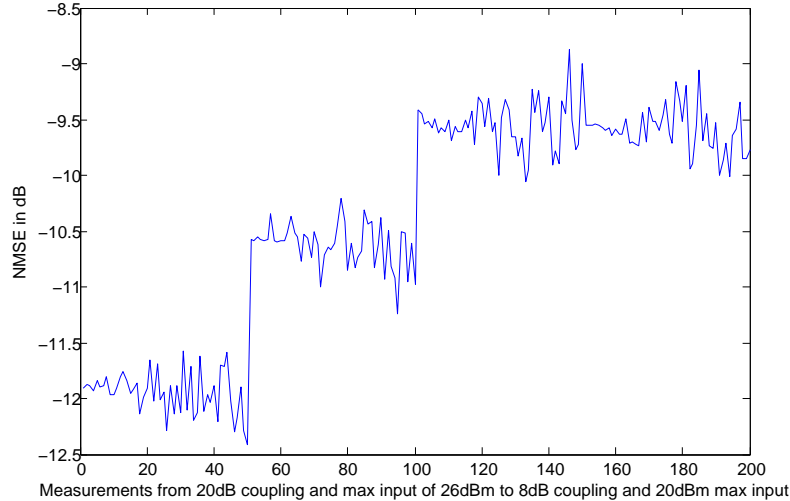


Figure 2.14: NMSE in dB for the Static model, calculated over the data series of the dynamic model extraction (here the static model is extracted through a spline using MATLAB)

the static model is not as accurate as the dynamic model. Indeed the dynamic model is fitted for modulated signal and particularly for the type of signal with similar statistics to the validation signal, whereas the (quasi) static PHD model is fitted for CW signals, thus giving the same importance to all power levels of the multi tone signal. Even though it is a simple model, fast to extract and easy to use, the static model is therefore not accurate enough to simulate the output of the PA with modulated signals as input signals.

2.5 Linearisation of the PA

In order to linearise the non-linear behavior of Power Amplifiers, Digital Pre Distorters (DPD) are commonly used in communication devices. This more or less complex structure is based on different algorithms to compensate for and linearise the PA non-linear effects. The input signal is first pre-distorted in the DPD and then goes through the PA. The PA can be then considered as linearised for the input signal. Transmitter linearity has always been of great interest as it gives a simple relation between the input and the output, which considerably ease signal treatment operated at the receiver side of the communication link.

In this project, one of the roles of the DPD will be to linearise the PA behavior when the latter is not under conditions of crosstalk. Thanks to this linearisation it will be possible to see the effect of the crosstalk better, particularly to see its consequences on spectral regrowth.

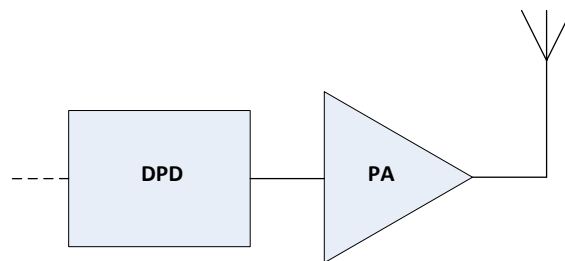


Figure 2.15: DPD within the transmitter architecture

2.5.1 Digital Pre Distorter for the PHD model

The DPD algorithm used in this part of the project is basic: the aim is to pre distort the signal enough in order to compensate the distortion of the amplifier (not including the distortion resulting

from the crosstalk, i.e. $A_2 = 0$). For this purpose the inverse function of the scattering functions $S_{21}(|A_1|)$ will be calculated, that means calculating the function S_{21}^{-1} which is the function expressing $|A_1|$ as function of $|B_2|$. This inverse function multiplied by the achievable gain $G_{slope} = \left| \frac{B_{2,max}}{A_{1,max}} \right|$ will allow us to linearise the amplitude response. Concerning the phase linearisation the aim is to keep the phase difference $\phi_{B_2} - \phi_{A_1}$ constant. By subtracting the phase shift $\phi_{S_{21}}$ introduced by the PA the phase difference is then kept constant and equal to zero. To sum up, the output x of the DPD can be expressed as:

$$x = DPD(A_1) = S_{21}^{-1}(G_{slope} \times |A_1|) \times e^{j(\phi_{A_1} - \phi_{S_{21}}(|A_1|))} \quad (2.25)$$

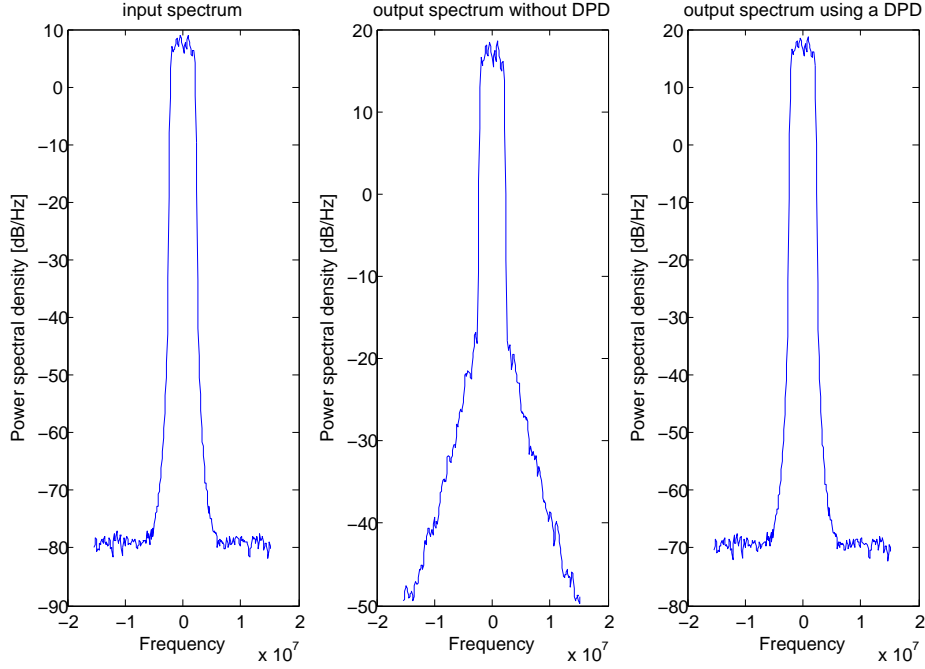


Figure 2.16: Effect of the DPD on the spectrum of the output signal of the PA, considering a WCDMA signal at the input

As we can see in figure 2.16, the DPD is very efficient to reduce the spectral regrowth and avoid most of the non-linear effect of the PA (not considering the crosstalk), and to linearise the output of the PA. The efficiency of this DPD is strongly linked to the simplicity of the static model. The DPD provides a significant help to the communications systems through linearising the PA output signal.

2.5.2 Digital Pre Distorter for the dynamic model

As the dynamic model is different from the static model, a new DPD must be designed to fit this model. Even if the basics are the same as for the static DPD, the method is slightly different. As for the static DPD, it is not possible to consider the effect of the incident wave A_2 and thus it will not appear in the dynamic DPD design. Thus, only the incident wave A_1 , which corresponds to the input signal, will be considered. The dynamic model can then be seen as $B_2 = H(A_1)\theta$. As the main aim of the DPD is to linearise the output of the PA, that also means inverting the model equation. The DPD design will be based on the indirect learning method reference, which means that we will first design a post distorter which will be the basis for the pre distorter. Starting from an input signal X , we first calculate the output Y of the PA. A post distorter block is applied for the normalised output Y_{DPD} , which is the normalised form of Y , and the target output of this post distorter is the normalised input X_{DPD} . That means that the post distorter block is the perfect inverter of the PA, except for a gain factor. The post distorter behavior can be described by $X_{DPD} = H(Y_{DPD})\theta_{DPD}$. This equation is the same as the one of the reduced dynamic model, except from the coefficients which are now θ_{DPD} . The DPD is then design with the same equation and the same coefficients θ_{DPD} . Figure 2.17 describes the process to design the DPD for this reduced dynamic model.

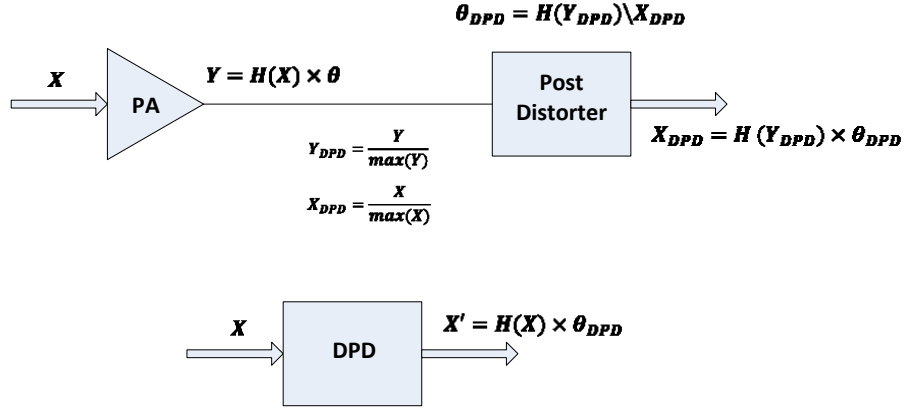


Figure 2.17: Indirect learning method to design the dynamic DPD

Sometimes it is better to proceed to a few iterations of this method to obtain better coefficients. Nevertheless in our case the iterations led to degraded spectral regrowth and that is why only one iteration of the method was sufficient to obtain the coefficients of the DPD.

2.6 Chapter summary

After having studied PA basics and the PA used and characterised for this project, we have presented two behavioral models for the PA, a static model and a dynamic one. The later is the most suitable and the more accurate to proceed to simulations and analyse the signal distortion due to crosstalk, and that is why it is this dynamic model which will be considered for MIMO simulations in the next parts of the project (except if specified). Thanks to DPDs it is possible to linearise the PA to observe the distortion generated by crosstalk and not by the PA non-linearities.

However, before modeling MIMO transmitters to analyse distortion due to crosstalk, a closer look on crosstalk is needed. As crosstalk in MIMO transmitters is mainly due to coupling between antennas, it is necessary to focus on antenna array theory to obtain coupling characteristics.

3 Antenna Design and Measurements

3.1 Microstrip antenna theory

In order to obtain accurate and realistic coupling values and in order to proceed to measurements involving a complete MIMO transmitter, we need to design antenna arrays for the MIMO. To keep it simple we decided to consider 2×2 MIMO transmitters, each defined by a two element antenna array. The choice of the designs has been based on simplicity of the design, easy manufacturing and the possibility to calculate both the S parameters of the network composed by the antennas and the far field; in our minds the best choice is to design patch antennas array. The patch antennas are easy to manufacture on a substrate and easily designed using Advanced Design System ¹. The design theory is described below.

3.1.1 Patch antenna design

The patch antennas will be implemented as microstrip lines on a substrate (typically 2 layers FR4) described by a relative permittivity ϵ_r , a loss tangent δ and a height h . The patch antennas to be resonant at a certain frequency f_{res} . The width of the patch can be expressed as [2]:

$$W = \frac{c}{2f_{res}} \sqrt{\frac{2}{\epsilon_r + 1}} \quad (3.1)$$

If $\frac{W}{h} \geq 1$ and $\epsilon_r \geq 1$, then most of the electric field lines concentrate in the substrate. But due to fringing, the micro strip line is electrically wider than physically, and thus some waves are travelling in the air before travelling in the substrate. That's why it is necessary to introduce a effective permittivity ϵ_{eff} to compensate the fringing.

$$\epsilon_{eff} = \frac{\epsilon_r + 1}{2} + \frac{\epsilon_r - 1}{2} \left(1 + 12 \frac{h}{W}\right)^{-\frac{1}{2}} [2] \quad (3.2)$$

A microstrip patch antenna is resonant at the frequency f_{res} when the microstrip line is $l = \frac{\lambda}{2}$ where λ is the wavelength. However, due to the fringing, the length of the patch is electrically longer than its physical dimensions of $2\Delta L$, ΔL being the extension on each side of the patch length (see figure 3.1)

$$\Delta L = 0.412h \left(\frac{\epsilon_{eff} + 0.3}{\epsilon_{eff} - 0.258} \right) \left(\frac{\frac{W}{h} + 0.262}{\frac{W}{h} + 0.813} \right) [10] \quad (3.3)$$

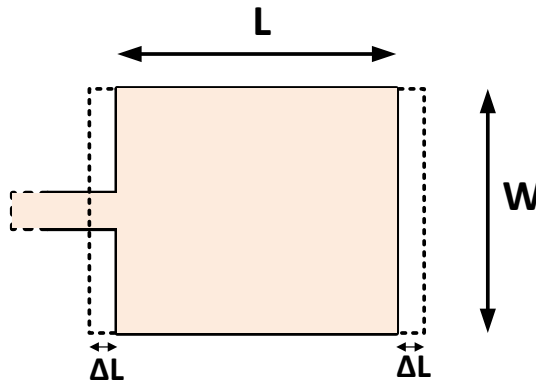


Figure 3.1: Antenna layout, physical and electrical length

¹Software of Agilent, <http://www.home.agilent.com/en/pc-1297113/advanced-design-system-ads>

In case of fringing the effective resonant length for a dominant TM_{010} mode is thus $L_{eff} = L + 2\Delta L$. For a dominant TM_{010} mode the resonant length is supposed to be $\frac{\lambda}{2}$, but in case of fringing the effective resonant length is equal to $L_{eff} = \frac{\lambda_{eff}}{2}$. So the relative length of the micro strip line is given by [10]:

$$L = \frac{c}{2f_{res}\sqrt{\epsilon_{eff}}} - 2\Delta L \quad (3.4)$$

where c is the speed of light in vacuum. The patch dimensions are then W and L .

3.1.2 Input impedance and inset feed

The designed antenna will have an input impedance. In an ideal case, the best would be to match this impedance to the characteristic impedance $Z_0 = 50\Omega$. The input impedance of the antenna can be calculated with the two slots model method for transmission lines, seen in figure 3.2. Each radiating slot of the micro strip antenna is represented by a parallel equivalent admittance $Y_i = G_i + B_i$, i being 1 or 2 depending on the slot position [2] [10]. The conductance G_1 of the first equivalent radiating slot can be obtained from the equation of the total radiated power P_{rad} :

$$G_1 = \frac{2P_{rad}}{|V_1|^2} \quad (3.5)$$

where V_1 is the voltage of the current source in the two slots model [10], and

$$P_{rad} = \frac{|V_1|^2}{120\pi^2} I_1$$

$$I_1 = \int_0^\pi \left(\frac{\sin\left(\frac{k_0 W}{2} \cos\theta\right)}{\cos\theta} \right)^2 \sin^3\theta d\theta = -2 + \cos(k_0 W) + k_0 W S_i(k_0 W) + \frac{\sin(k_0 W)}{k_0 W} \quad [2]$$

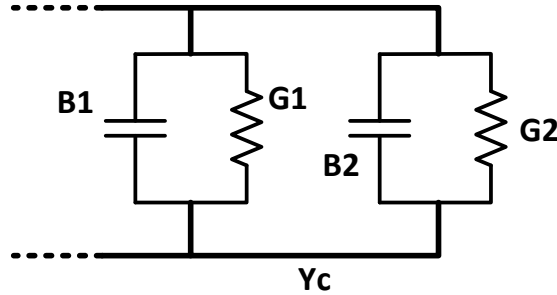


Figure 3.2: Two slots model for a transmission line (Y_c is the line impedance)

From this point it is possible to calculate the total resonant input admittance Y_{in} , equal to the sum of the admittance of the two slots: $Y_{in} = Y_1 + Y_2 = 2G_1$, as $Y_2 = G_1 - jB_1$ because of the $\lambda/2$ transmission line between the two slots. The resonant input resistance can be thus calculated through the equation

$$R_{in} = \frac{1}{2(G_1 \pm G_{12})} \quad (3.6)$$

where G_{12} is the mutual conductance. The + sign corresponds to our case, odd resonant voltage distribution between the slots which is the case of the TM_{010} mode we considered (the - sign corresponds to even distribution).

$$G_{12} = \frac{1}{120\pi^2} \int_0^\pi \left(\frac{\sin\left(\frac{k_0 W}{2} \cos\theta\right)}{\cos\theta} \right)^2 J_0(k_0 L \sin\theta) \sin^3\theta d\theta \quad [2] \quad (3.7)$$

where J_0 is the Bessel function of first kind at the order zero. Most of the time, the mutual conductance between the slots is considered small relative to the self conductance G_1 . It is shown in [2] that

designing a recessed micro strip line feed (also called inset feed) up to a distance y_0 inside the microstrip antenna is a good solution to match the antenna input to the feeding line. The new layout of the antenna is displayed in figure 3.3.

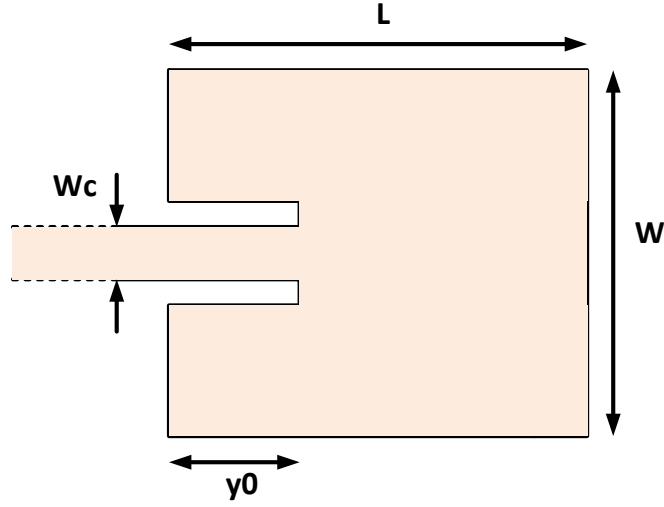


Figure 3.3: New design of the antenna including the inset feed line

Assuming that the width W_{feed} of the micro strip feed is bigger than the height h of the substrate, the characteristic impedance Z_c of the line can be described as [3]

$$Z_c = \frac{120\pi}{\sqrt{(\epsilon_{eff}) \left(\frac{W_{feed}}{h} + 1.393 + 0.667 \ln \left(\frac{W_{feed}}{h} + 1.444 \right) \right)}} \quad (3.8)$$

If we assume that $G_1 Z_c \ll 1$ and $B_1 Z_c \ll 1$ we can express the input resonant impedance of the micro strip at a distance y_0 of the edge, where the intersection with the inset feed occurs:

$$R_{in}(y = Y_0) = R_{in} \cos \left(\frac{\pi}{L} y_0 \right)^2 \quad (3.9)$$

Thanks to this inset feed, the patch antenna can be matched to the impedance Z_c of the micro strip line (typically 50Ω).

3.2 Antenna layout and manufacturing requirements

Based on the fundamental theory developed in section 3.1, three different two element antenna arrays have been designed using Agilent softwares ADS² and Momentum³. The designs are only different in the distance between the two antenna centers, and except from that the antenna dimensions are exactly the same. The reason for different distances between antenna centres is to obtain various coupling between the antennas of the array: a strong coupling, a low coupling, and very low coupling (which can be seen as a reference). The antennas will be manufactured as PCBs at the company Sunstone Circuits[®]⁴. The requirements on the substrate and on the design will thus be the following: the substrate should be double copper layer FR-4 (good enough for such microstrip antennas and cheaper than Rogers dielectric material), the thickness is about 62 mil ($h = 62\text{mil}$) and the minimum distance between edges should be 6 mil. The permittivity of the substrate is around $\epsilon_r = 4.5$. The substrate characteristics are presented below:

$$\epsilon_r = 4.5$$

$$h = 62\text{mil}$$

²<http://www.home.agilent.com/en/pc-1297113/advanced-design-system-ads>

³<http://www.home.agilent.com/en/pc-1887116/momentum-3d-planar-em-simulator>

⁴<http://www.sunstone.com/QuoteQT.aspx>

According to this requirements and to the formulas presented on section 3.1 the dimensions of a single antenna for a resonant frequency $f_r = 2.14\text{GHz}$ are the following:

$$L = 3.22\text{cm}$$

$$W = 4.23\text{cm}$$

$$W_{feed} = 2.37\text{mm}$$

$$y_0 = 1.20\text{cm}$$

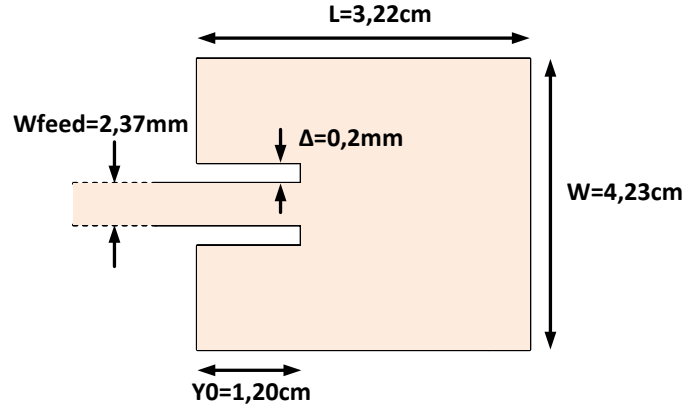


Figure 3.4: Dimensions of the designed antenna layout

The design of a single antenna and the layout designed in ADS are presented in figure 3.4 and in appendix C. When simulating these designs on ADS and Momentum, we can see that the resonant frequency is not exactly the desired one: whereas the antenna has been designed for 2.14GHz , the simulation on ADS and Momentum shows that the antenna is resonant at 2.17GHz . This difference can be explained by the substrate definition (maybe not accurate enough) and by some approximations assumed in the formulas of section 3.1. A few improvements are thus necessary to improve the antenna design, particularly on the length L of the micro strip antenna. However the characteristics of the FR-4 substrate provided by Sunstone may also be slightly different from the values we considered in the simulation ($\epsilon_r = 4.5 \pm 0.1$ and $h = 61 \pm 6\text{ mil}$) and as the main aim of this thesis is the study of the coupling between the transmitting antennas, the small change in frequency is not critical. To avoid time consuming improvements, we chose to keep the initial design: the signal will be adapted later to the resonant frequency of the antenna. Once manufactured, the feed lines of the arrays are soldered to a SMA end launch connector. The final arrays can be seen on figure 3.6, and the simulated radiation pattern is shown in figure 3.5. Details about the radiated E-field in the E-plane and the H-plane can be found in appendix C.

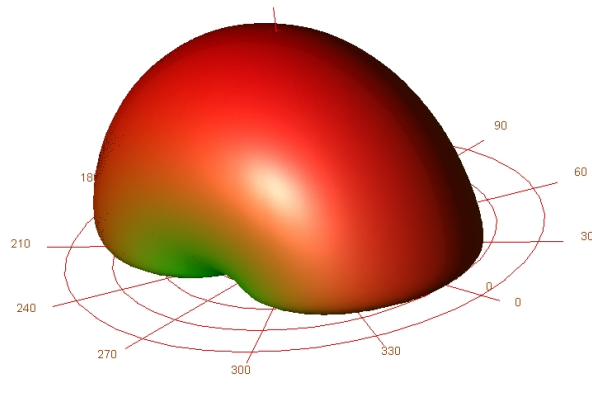


Figure 3.5: Simulated radiation pattern of one of the arrays (medium coupling, 0.429λ between patch centres)



Figure 3.6: Manufactured antenna arrays: 3 different designs for 3 different coupling values

3.3 Antenna measurements

The arrays are tested as two ports networks with a Network Analyser (E8361A from Agilent) to measure accurately the real S-parameter. As the designed arrays are symmetrical and reciprocal, the parameters S_{11} and S_{12} equal the parameters S_{22} and S_{21} , respectively. We are here particularly interested in the S parameters S_{11} and S_{12} because they represent the reflected wave due to the error in the matching of the antenna input port and the wave coming from the coupling between the two antennas, respectively: $A_1 = S_{11}B_1 + S_{12}B_2$.

The S parameters for the three arrays are displayed in figure 3.7 and 3.8. We can first observe that the resonant frequency is neither the designed resonant frequency (2.14GHz) nor the simulated one (2.17GHz) but 2.12GHz. This can be explained as aforementioned by the fluctuating characteristic of the FR-4 substrate from Sunstone. The measured characteristics are nevertheless good: S_{11} is below -28dB at 2.12GHz for the three arrays, which is a proof of good matching, and S_{12} at 2.12GHz corresponds to what have been simulated before. The table 3.1 summarizes the coupling between the antennas for the different designs.

Table 3.1: Coupling between the different array designs

	Distance to centres (mm)	Distance to centres ($1/\lambda$)	Simulated S_{12} (dB) at 2.17GHz	Measured S_{12} (dB) at 2.12GHz
d1	49.5	0.350	-14.76	-13.98
d2	60.7	0.429	-21.90	-20.86
d3	83.0	0.587	-30.25	-28.39

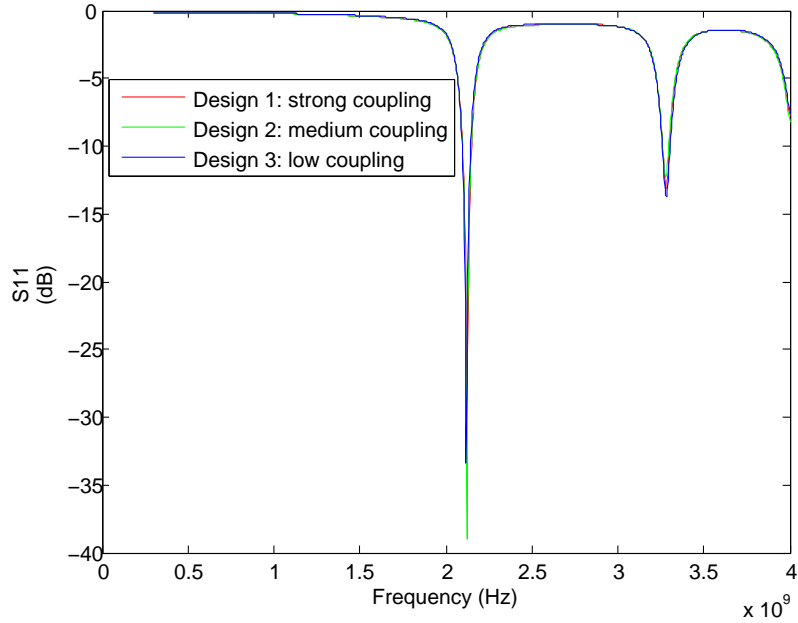


Figure 3.7: Measured S_{11} for the three designs. Red for strong coupling, green for medium coupling and blue for low coupling

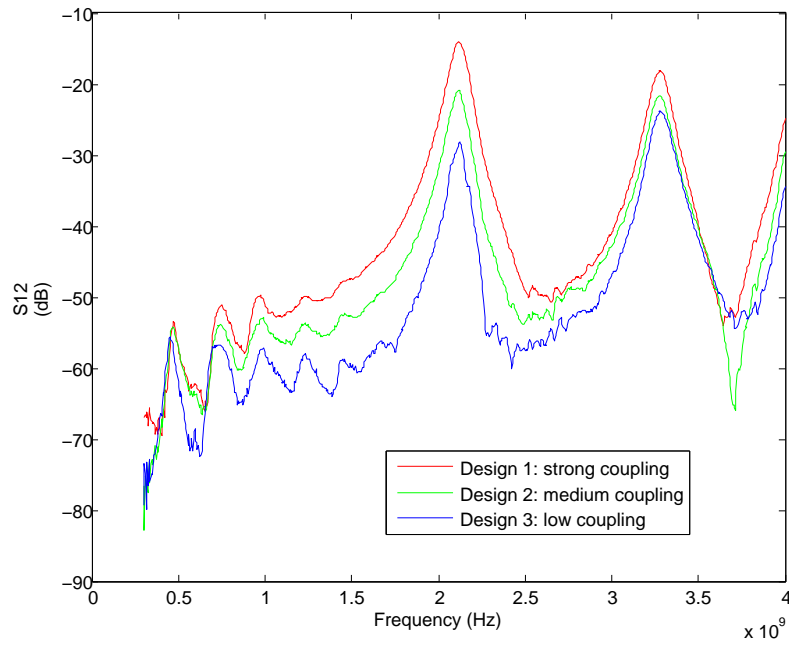


Figure 3.8: Measured S12 for the three designs. Red for strong coupling, green for medium coupling and blue for low coupling

4 Crosstalk distortion analysis

We have so far developed behavioral models with dual-input for the PA and we have designed various two-element antenna arrays to obtain accurate S-parameter and particularly different coupling between antennas. It is now possible to link these two elements, the PA model and the S-parameter of the antenna array, in order to simulate a MIMO transmitter. In this section we will thus develop $N \times N$ MIMO transmitter models in order to analyse the distortion of the output signal due to crosstalk between antennas.

Assuming a model for the power amplifiers in the $N \times N$ MIMO, it is first possible to simulate only the PA part, considering an ideal coupling between ideal antennas. Then the S-parameters of the N -port network formed by the N antennas can be integrated in the simulation to analyse in a more realistic way, the distortion due to crosstalk. In this study of the contribution of crosstalk to signal distortion, we will focus on a transmitter of a 2×2 MIMO. However, as seen in figure 4.4, it is a first step toward MIMO transmitters with more antennas.

4.1 Notations

In the case of a transmitter in a $N \times N$ MIMO, $A_{1,i}$, $A_{2,i}$ and $B_{2,i}$ are the ordinary incident voltage wave, the back-coming incident voltage wave and the scattered voltage wave of the i^{th} branch of the transmitter, respectively. For the transmitter of a 2×2 MIMO, $A_{1,1}$, $A_{2,1}$ and $B_{2,1}$ are thus the voltage waves involved in the first branch of the transmitter, and $A_{1,2}$, $A_{2,2}$ and $B_{2,2}$ are the voltage waves involved in the second branch of the transmitter. This notation is also explained in appendix A.4.

4.2 Ideal coupling and simple MIMO model

4.2.1 Ideal coupling

Ideal coupling can be described as the coupling between perfectly matched antennas. This means that no wave is reflected by the antenna toward the PA, and the incident wave $A_{2,1}$ is only function of the output wave of the second transmitter due to the coupling. As depicted in figure 4.1, this ideal coupling is thus considered as linear and can be expressed by a factor $\alpha_{coupling}$ between $A_{2,1}$, incident back-coming wave in the first branch of the MIMO, and $B_{2,2}$, output wave of the second branch of the MIMO transmitter:

$$A_{2,1} = \alpha_{coupling} B_{2,2} \quad (4.1)$$

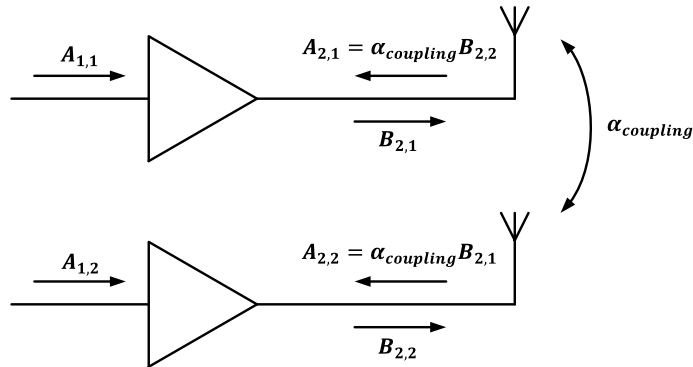


Figure 4.1: Description of ideal coupling for a 2×2 MIMO transmitter with a coupling factor $\alpha_{coupling}$ between the two branches

4.2.2 Time delay MIMO model

A simple MIMO simulation can be set up: the easiest is to consider a time delay for the wave propagation between the two antennas: the output $B_{2,1}$ of the antenna 1 at the time n becomes the incident wave $A_{2,2}$ for the antenna 2 at the time $n + 1$, and vice versa. Simulating the transmitted signal time

step by time step and considering the fixed coupling factor α , it is possible to obtain the spectrum of the signal at the output of the two antennas. For this simple MIMO transmitter model, the PA will be modeled by the PHD model. To observe the output spectrum a modulated signal is needed. The modulated signal considered is a WCDMA signal. This WCDMA signal has a signal bandwidth of 3.84MHz for a 5MHz channel bandwidth. The oversampling rate is 8 and the signal will be considered at 2.14GHz.

In order to observe the spectral regrowth due to crosstalk between the antennas and avoid spectral regrowth due to the non linearities of the PA, the DPD developed for the static model in section 2.5.1 is used. As aforementioned in section 2.5.1, the DPD is very efficient thanks mainly to the simplicity of the static model. Indeed, the output spectrum of the signal is a spectrum like the input signal spectrum, but without spectral regrowth and with the expected gain.

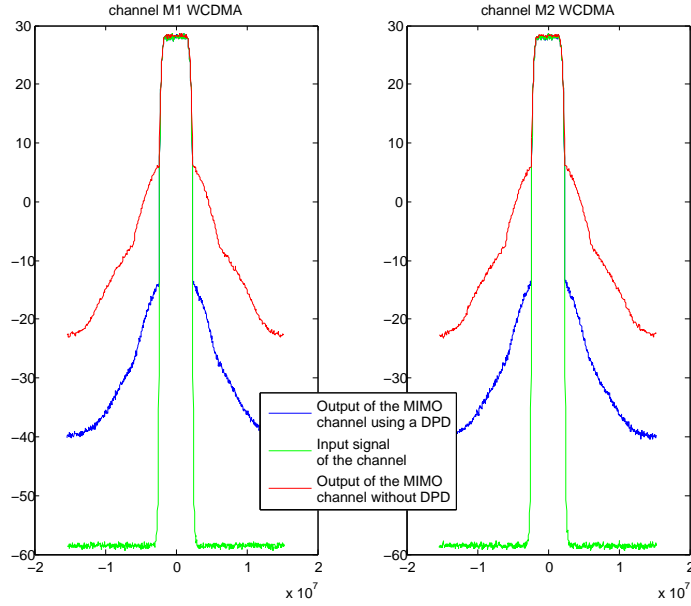


Figure 4.2: Spectrum of the signal on the two channels (channel 1 on the left, channel 2 on the right) of the MIMO transmitter, with DPD (in blue) and without a DPD (in red). Spectrum of the input signal is displayed in blue. A coupling factor of -14dB between the antennas has been used

Looking at the effect of the DPD without considering crosstalk (figure 2.16), we can see that there is barely any spectral regrowth. So, assuming that the incident wave $A_{2,1}$ (or $A_{2,2}$) is entirely coming from the coupling between the antennas, we can say that the spectral regrowth seen on the output spectrum on figure 4.2 is mainly due to crosstalk effect.

4.2.3 Distortion analysis and ACLR

A good way to calculate the contribution of crosstalk on signal distortion is to calculate the adjacent channel leakage ratio (ACLR), described in appendix A.5.3. The ACLR will depend on the ideal coupling factor $\lambda_{coupling}$ between the antennas (as aforementioned in section 4.2.1). In figure 4.3 the simulated ACLR for different coupling factors between the antennas is plotted as function of the coupling. As aforementioned in appendix A.5.3, the 3GPP standard requirements for the ACLR is at least -45dB . That means that above this limit ($\text{ACLR} > -45\text{dB}$) the requirements are not fulfilled and the crosstalk effect cannot be negligible. In our case, this limit corresponds to a coupling factor between the antennas of -12.4dB . Even if this simulation is limited by the simplicity of the MIMO model and by many assumptions we made concerning the ideal coupling, this -12.4dB value is a good indicator of the maximum achievable coupling in the MIMO system. However, thanks to the S-parameter of the antenna arrays and the dynamic model, more accurate simulations are achievable.

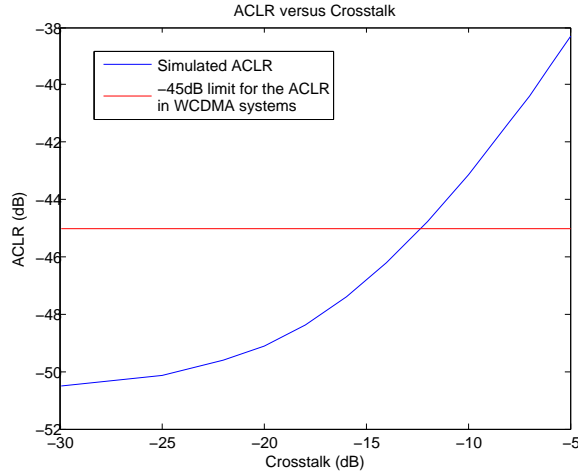


Figure 4.3: Simulated ACLR for the output of a MIMO channel under condition of crosstalk. In red, the -45dB limit for WCDMA communication systems

4.3 MIMO model with antennas

4.3.1 MIMO model and equations

Considering now a more realistic coupling, based on the measured S-parameters of the designed antennas, the wave $A_{2,1}$ is not only function of $B_{2,2}$ but also function of $B_{2,1}$, according to the equations in appendix A.2.

$$A_{2,1} = S_{11}B_{2,1} + S_{12}B_{2,2} \quad (4.2)$$

The coupling cannot be considered as ideal any more, even if the contribution of $A_{2,1}$ coming from the second branch of the MIMO, $S_{12}B_{2,2}$, is bigger than the contribution due to mismatch, $S_{11}B_{2,1}$. Whereas in the previous section the PHD model was used and a time delay was included between the two branches of the MIMO, it is more realistic to use the developed dynamic model for the PA to simulate the PA behavior more accurately.

Moreover, instead of introducing a unit time delay for propagation between the antennas, the equations of the two branches of the MIMO will be solved jointly as a complete system, and so without any delay for propagation. This choice is made first because of the small propagation time between the two antennas considering how close they are to each other in the designed arrays (0.277ns propagation time between antenna centres for the array with the biggest distance), and secondly because the S-parameters of the antenna arrays seen as 2 ports networks already include phase delay in addition to coupling. Then the output of the PA, B_{21} , B_{22} and more generally $B_{2,i}$ for the i^{th} branch of a $N \times N$ MIMO transmitter, must be calculated in the same time and as a system of equations, as it is shown in figure 4.4.

Considering the dynamic model and the i^{th} branch of a $N \times N$ MIMO transmitter, (2.24) can also be written in a way that reminds the PHD model basis: $B_{2,i}$ can be expressed as the sum of 3 functions, the first one composed by terms relying only on $A_{1,i}$ and its memory but also the terms including the memory of $A_{2,i}$ or $A_{2,i}^*$, the second one gathering the terms involving $A_{2,i}$, and the last one gathering the terms involving $A_{2,i}^*$, as it is stated for the PHD model in (2.13). The aim of using this form for the dynamic model is to separate the terms depending on $A_{2,i}$ from the others, to solve the system in an easier way: it is in fact only a factorisation in $A_{2,i}$ and $A_{2,i}^*$. It is developed in (4.3)

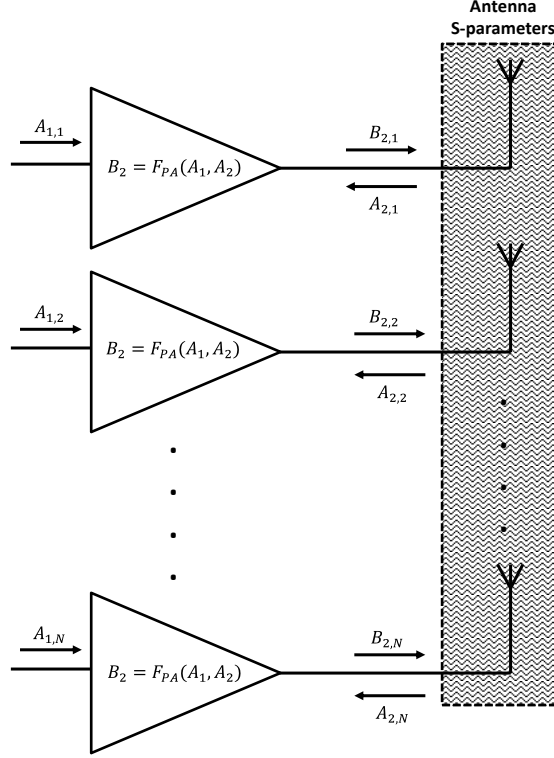


Figure 4.4: MIMO model representation: solving the $B_{2,i}$ as unknowns of a system of equations

below for a 2×2 MIMO transmitter:

$$\begin{aligned}
 \begin{bmatrix} B_{2,1} \\ B_{2,2} \end{bmatrix} &= \begin{bmatrix} H_1(A_{1,1}) & \cdots & H_P(A_{1,1}) \\ H_1(A_{1,2}) & \cdots & H_P(A_{1,2}) \end{bmatrix} \begin{bmatrix} \theta_1 \\ \vdots \\ \theta_P \end{bmatrix} \\
 &+ \begin{bmatrix} S_{22}(A_{1,1}) & 0 \\ 0 & S_{22}(A_{1,2}) \end{bmatrix} \begin{bmatrix} A_{2,1} \\ A_{2,2} \end{bmatrix} \\
 &+ \begin{bmatrix} T_{22}(A_{1,1}) & 0 \\ 0 & T_{22}(A_{1,2}) \end{bmatrix} \begin{bmatrix} A_{2,1}^* \\ A_{2,2}^* \end{bmatrix} \quad (4.3)
 \end{aligned}$$

where the matrices $H_i(A_{1,N})$ express the terms of degree i from (2.18) (typically $A_{1,N}(t-q\Delta)|A_{1,N}(t-q\Delta)|^{2(i-1)}$ for the branch N of the MIMO transmitter; $S_{22}(A_{1,N})$ corresponds to the factorisation in A_2 of the terms from (2.19) depending on A_2 (the sum of terms like $\theta_{r,q,l}|A_{1,N}(t-q\Delta)|^{2(l-1)}$); finally $T_{22}(A_{1,N})$ corresponds to the factorisation in A_2^* of the equation (2.19) (terms like $\theta_{r,q,l}A_{1,N}^2(t-q\Delta)|A_{1,N}(t-q\Delta)|^{2(l-2)}$). The matrices $H_i(A_{1,i})$ and the terms $S_{22}(A_{1,i})$ and $T_{22}(A_{1,i})$ are developed below:

$$H_1(A_{1,i}) = [A_{1,i}(t) \quad A_{1,i}(t-\Delta) \quad \cdots \quad A_{1,i}(t-Q\Delta)] \quad (4.4)$$

$$H_2(A_{1,i}) = [A_{1,i}(t)|A_{1,i}(t)|^2 \quad A_{1,i}(t-\Delta)|A_{1,i}(t-\Delta)|^2 \quad \cdots \quad A_{1,i}(t-Q\Delta)|A_{1,i}(t-Q\Delta)|^2] \quad (4.5)$$

$$\begin{aligned}
 H_P(A_{1,i}) &= [A_{1,i}(t)|A_{1,i}(t)|^{2(P-1)} \quad A_{1,i}(t-\Delta)|A_{1,i}(t-\Delta)|^{2(P-1)} \\
 &\quad \cdots \quad A_{1,i}(t-Q\Delta)|A_{1,i}(t-Q\Delta)|^{2(P-1)}] \quad (4.6)
 \end{aligned}$$

$$\begin{aligned}
S_{22}(A_{1,i}) &= \theta_{0,0,1} + \theta_{0,0,2}|A_{1,i}(t)|^2 + \cdots + \theta_{0,0,L}|A_{1,i}(t)|^{2(L-1)} \\
&\quad + \theta_{0,1,2}|A_{1,i}(t-\Delta)|^2 + \cdots + \theta_{0,1,L}|A_{1,i}(t-\Delta)|^{2(L-1)} \\
&\quad + \cdots \\
&\quad + \theta_{0,Q,2}|A_{1,i}(t-Q\Delta)|^2 + \cdots + \theta_{0,Q,L}|A_{1,i}(t-Q\Delta)|^{2(L-1)} \quad (4.7)
\end{aligned}$$

$$\begin{aligned}
T_{22}(A_{1,i}) &= \theta_{0,0,1}A_{1,i}^2(t) + \theta_{0,0,2}A_{1,i}^2(t)|A_{1,i}(t)|^2 + \cdots + \theta_{0,0,L}A_{1,i}^2(t)|A_{1,i}(t)|^{2(L-1)} \\
&\quad + \theta_{0,1,1}A_{1,i}^2(t-\Delta) + \theta_{0,1,2}A_{1,i}^2(t-\Delta)|A_{1,i}(t-\Delta)|^2 + \cdots + \theta_{0,1,L}A_{1,i}^2(t-\Delta)|A_{1,i}(t-\Delta)|^{2(L-1)} \\
&\quad + \cdots \\
&\quad + \theta_{0,Q,1}A_{1,i}^2(t-Q\Delta) + \theta_{0,Q,2}A_{1,i}^2(t-Q\Delta)|A_{1,i}(t-Q\Delta)|^2 + \cdots + \theta_{0,Q,L}A_{1,i}^2(t-Q\Delta)|A_{1,i}(t-Q\Delta)|^{2(L-1)} \quad (4.8)
\end{aligned}$$

When coming to memory considerations, all the terms in (2.18) and (2.19) with $A_2(t-q\Delta)$ or $A_2^*(t-q\Delta)$ and $q \neq 0$ (so all the terms relying on A_2 or A_2^* memory) can be included in the matrices H_i and are considered as known constants.

(4.3) can be thus written in a simplified matrix form:

$$\mathbf{b}_2 = \mathbf{H}(\mathbf{a}_1)\Theta + \mathbf{S}_{22}(\mathbf{a}_1)\mathbf{a}_2 + \mathbf{T}_{22}(\mathbf{a}_1)\mathbf{a}_2^* \quad (4.9)$$

where

$$\begin{aligned}
\mathbf{b}_2 &= [B_{2,1} \ B_{2,2}]^T \\
\mathbf{a}_1 &= [A_{1,1} \ A_{1,2}]^T \\
\mathbf{a}_2 &= [A_{2,1} \ A_{2,2}]^T
\end{aligned}$$

From appendix A.2, we can also write the relation between \mathbf{a}_2 and \mathbf{b}_2 concerning the antenna S-parameters \mathbf{S}_{ant} :

$$\mathbf{a}_2 = \mathbf{S}_{\text{ant}}\mathbf{b}_2 \quad (4.10)$$

And inserting (4.10) in (4.9):

$$\mathbf{b}_2 = \mathbf{H}(\mathbf{a}_1)\Theta + \mathbf{S}_{22}(\mathbf{a}_1)\mathbf{S}_{\text{ant}}\mathbf{b}_2 + \mathbf{T}_{22}(\mathbf{a}_1)\mathbf{S}_{\text{ant}}^*\mathbf{b}_2^* \quad (4.11)$$

Separating \mathbf{b}_2 in real and imaginary parts $\mathbf{b}_2 = \mathbf{b}_r + j\mathbf{b}_i$, (4.11) is now a system of equations depending on \mathbf{b}_2 possible to solve in MATLAB.

$$\begin{aligned}
\begin{bmatrix} \mathbf{b}_r \\ \mathbf{b}_i \end{bmatrix} &= \begin{bmatrix} I - \Re(\mathbf{S}_{22}(\mathbf{a}_1)\mathbf{S}_{\text{ant}}) - \Re(\mathbf{T}_{22}(\mathbf{a}_1)\mathbf{S}_{\text{ant}}^*) & \Im(\mathbf{S}_{22}(\mathbf{a}_1)\mathbf{S}_{\text{ant}}) - \Im(\mathbf{T}_{22}(\mathbf{a}_1)\mathbf{S}_{\text{ant}}^*) \\ -\Im(\mathbf{S}_{22}(\mathbf{a}_1)\mathbf{S}_{\text{ant}}) - \Im(\mathbf{T}_{22}(\mathbf{a}_1)\mathbf{S}_{\text{ant}}^*) & I - \Re(\mathbf{S}_{22}(\mathbf{a}_1)\mathbf{S}_{\text{ant}}) + \Re(\mathbf{T}_{22}(\mathbf{a}_1)\mathbf{S}_{\text{ant}}^*) \end{bmatrix}^{-1} \\
&\quad \times \begin{bmatrix} \Re(\mathbf{H}(\mathbf{a}_1)\Theta) \\ \Im(\mathbf{H}(\mathbf{a}_1)\Theta) \end{bmatrix} \quad (4.12)
\end{aligned}$$

The real and imaginary parts of \mathbf{b}_2 can thus be solved and the output of the two power amplifiers of the MIMO transmitter can be thus calculated.

4.3.2 Crosstalk distortion

The same WCDMA signal used in section 4.2.2 is used as input for this more complex MIMO transmitter model. The input signal for the first branch of the MIMO transmitter is independent from the input signal inserted in the second branch. Using the dynamic model previously developed with $P = 4$, $L = 2$ and $Q = 2$, we first obtain the coefficients to model the behavior of the PA. The S-parameter of the antennas can be either obtained through ADS simulations or the S-parameters measured from the designed microstrip arrays. From now on we will use the S-parameters measured (see section 3.3), in order to perform measurements later. The frequency is then set to 2.12GHz instead of 2.14GHz. This

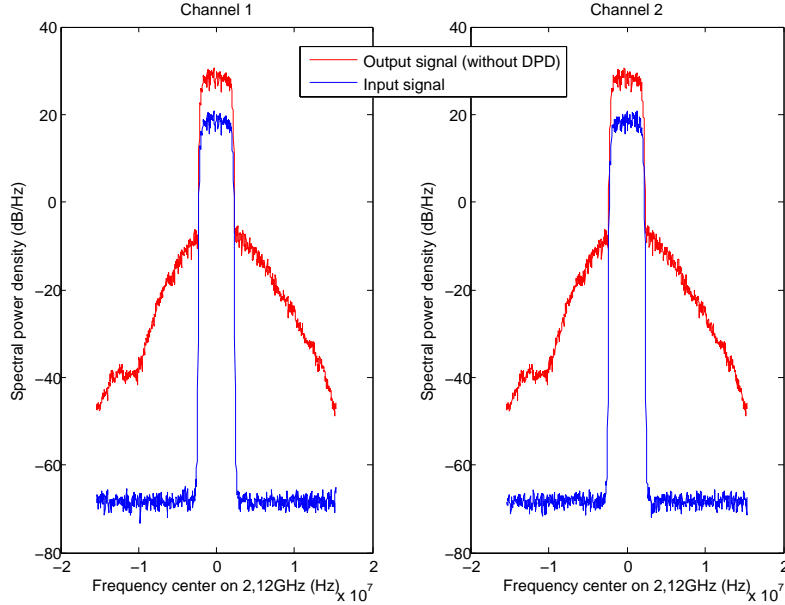


Figure 4.5: Spectrum of the output and input signals from the MIMO transmitter without DPD (on the left: branch 1; on the right: branch 2)

change in frequency results in minor changes concerning the PA behavior, as explained in section 2.2.2. With the WCDMA signal at the input of the 2×2 MIMO and without DPD, the output spectrum of the complete output signal can be seen in figure 4.5.

Without a DPD, the spectrum is distorted and it is not possible to distinguish which part of the spectral regrowth is due to the crosstalk or due to the non-linearities of the PA. Therefore two solutions are possible: using a DPD adapted to the dynamic model (see section 2.5.2) or separate and analyse the contribution from crosstalk. Indeed when looking at (4.11), it is possible to separate the part of the output signal depending on \mathbf{a}_2 (or \mathbf{a}_2^*) and the part independent from \mathbf{a}_2 . Looking only at the spectrum of the part depending on \mathbf{a}_2 , $S_{22}(\mathbf{a}_1)\mathbf{a}_2 + T_{22}(\mathbf{a}_1)\mathbf{a}_2^*$ in (4.11), we will highlight the contribution of crosstalk to the signal distortion. The remaining term $\mathbf{H}(\mathbf{a}_1)\Theta$ is only dependent on \mathbf{a}_1 and the distortion resulted from this term is representative of the contribution from the non linearities of the PA.

Using the DPD developed in the previous section 2.5.2, the spectral regrowth (see figure 4.6) from distortion due to crosstalk can be analysed for the 3 different manufactured antennas.

The spectrum of the output signal due only to the crosstalk is presented in figure 4.7, and the comparison with the output signal using a DPD is presented in figure 4.8.

As we can see, the output spectrums are similar (see figure 4.8), except in the main channel bandwidth where the PSD of the spectrum resulting from the use of a DPD (straight lines) is higher than the PSD corresponding to the crosstalk (dashed lines). This can be explain by the fact that the crosstalk contribution induce no gain in the main channel bandwidth.

We are however more interested in the PSD in the adjacent channels bandwidth. A detailed plot in figure 4.9 presents the lower part of the main channel and the lower adjacent channel. If we focus the comparison between -2.5MHz and -7.5MHz from the center of the main channel, we can see that the spectrum resulting from the use of the DPD and the spectrum resulting from the crosstalk only are diverging. Indeed the PSD from the contribution of crosstalk is lower than the PSD of the complete output signal, and the difference increases when the coupling decreases. This means the two PSD are very close for a high coupling, and are diverging for a lower coupling. Moreover, the difference between these PSD is smaller on the part of the adjacent channel close to the central frequency (in figure 4.9 it corresponds to the left part of the spectrum, close to -2.5MHz), where the spectral regrowth is usually bigger.

These observations can be explained by the limited abilities of the DPD to linearise the PA. If the DPD can't linearise the PA enough in order to reduce the distortion due to classic non-linearities of the PA below the level of distortion resulting from the crosstalk contribution, the PSD in the adjacent

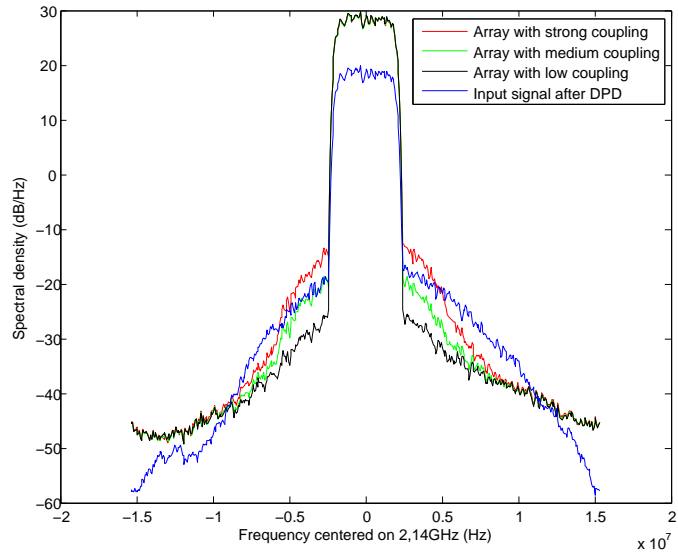


Figure 4.6: Spectrum of the output signal for different array designs (red:strong coupling; green: medium coupling; black:low coupling) and spectrum of the input signal after the DPD

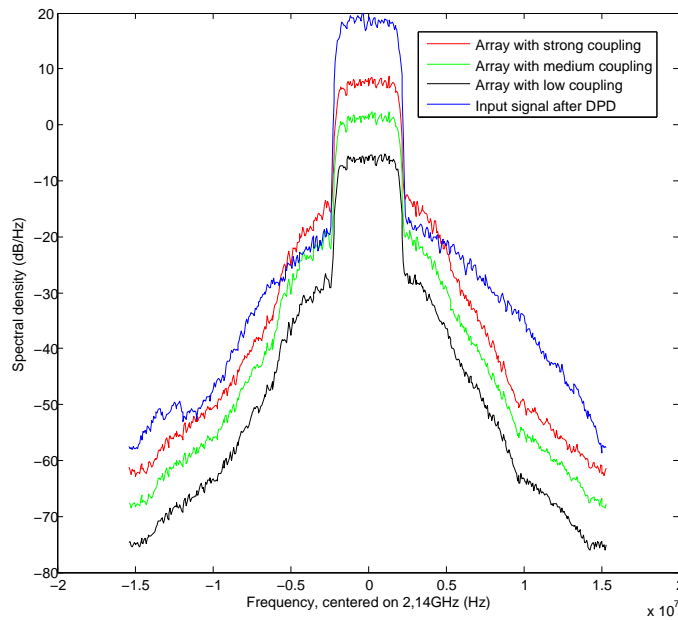


Figure 4.7: Spectrum of the output signal coming only from crosstalk for different array designs (red:strong coupling; green: medium coupling; black:low coupling)

channel will correspond to the contribution to distortion from the non-linearities of the PA. However, if the DPD linearise the PA enough, the spectral regrowth will correspond to the contribution of crosstalk to distortion. In our case the DPD is thus not good enough, that's why from here onwards only the contribution to crosstalk is considered.

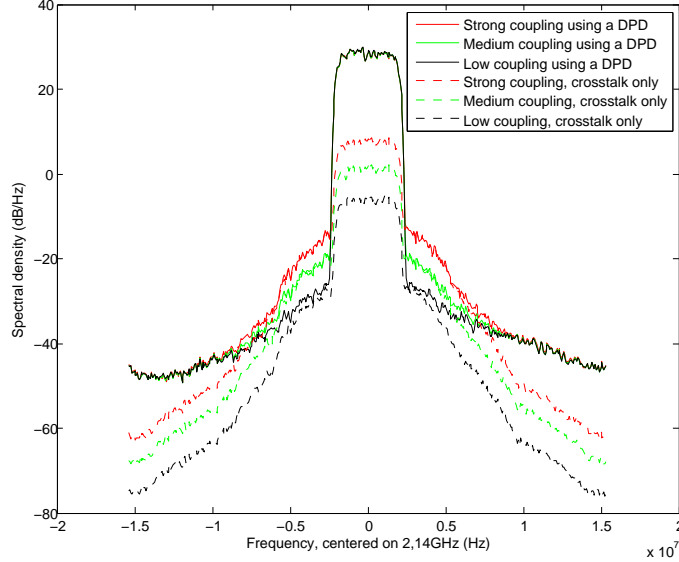


Figure 4.8: Comparison of the output spectrum considering the complete signal and using a DPD (straight lines) and the contribution from crosstalk (dashed lines) for different array design (red:strong coupling; green: medium coupling; black:low coupling)

The ACLR (see appendix A.5.3) is commonly use to estimate the distortion of the signal. Obtaining the output spectrum, it is easy to calculate the ACLR. Results for ACLR calculations are presented in the table 4.1 below. The first observations when looking at the table is that the ACLR calculated for the complete signal using a DPD and the ACLR calculated from the crosstalk contribution are almost the same for strong and medium coupling (d1 and d2), only a few tenths of decibel, but are diverging when the coupling between the antennas gets lower. This observation confirms the statement previously made about the efficiency of the DPD, efficient enough to see the distortion due to crosstalk when the coupling is significant, but not good enough when the coupling decreases.

As expected, the ACLR worsens when the coupling increases, which confirms that the output signal of the PA is distorted under conditions of crosstalk. Moreover, the ACLR in dB seems to increase linearly (in dB) with the coupling. This is however not the case any more when the whole output signal is considered (using the DPD). But the shape of the curve is very close to a straight line, which also means that the coupling and the distortion (at least the ACLR) are linearly dependent. The linear ratio would be 0.978, and thus the -45dB limit for ACLR in WDCMA transmitters (see appendix A.5.3) would be reach at about -11.6dB coupling.

Table 4.1: ACLR between the different array designs

	Measured S_{12} (dB) at 2.12GHz	ACLR (dB)		
		complete signal without DPD	complete signal with DPD	crosstalk distortion
d1	-13.98	-38.99	-47.57	-47.29
d2	-20.86	-39.16	-53.78	-54.29
d3	-28.39	-39.43	-58.83	-61.39

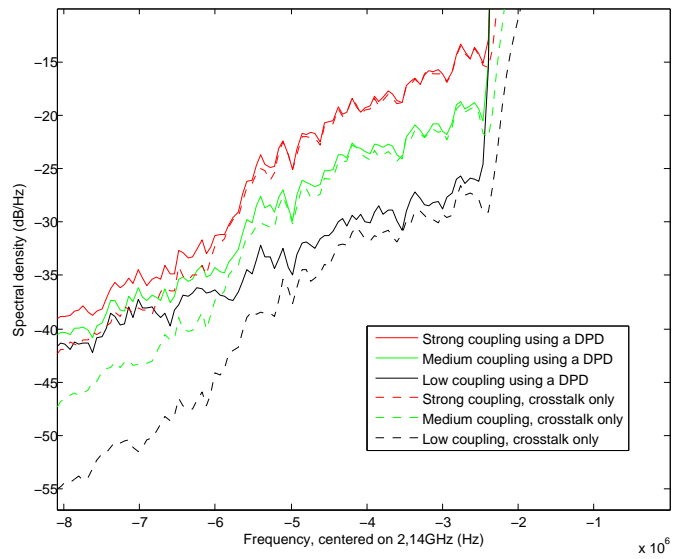


Figure 4.9: Detail of figure 4.8 showing the spectrum on the lower adjacent channel channel (from -2.5MHz to -7.5MHz)

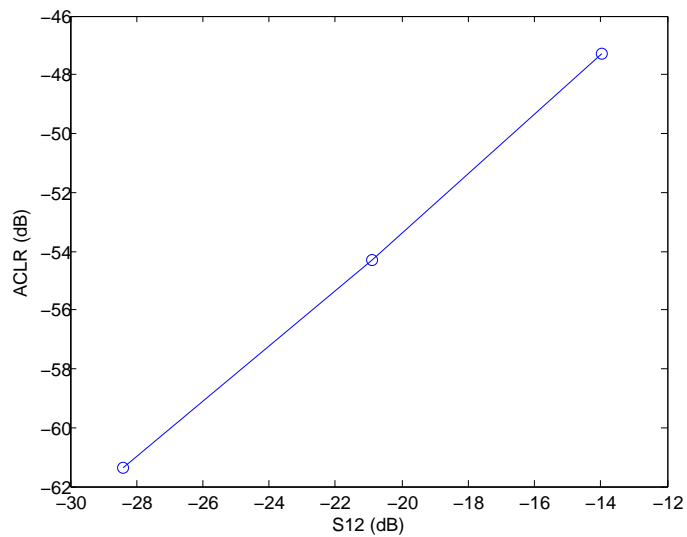


Figure 4.10: ACLR as function of the coupling S_{12} between the antennas

4.3.3 Comparison with ideal coupling

When comparing these results on ACLR with the results found when using the PHD model for the PA in an ideal coupling time delayed MIMO, a few differences are distinguishable (see figure 4.11). First, both the ACLR for the complete signal and the ACLR with crosstalk contribution only calculated with the latest developed MIMO model are better (so lower) of at least 1dB (for a coupling of -14dB ; delta is 11dB for a coupling of -28dB). This can be explained by the assumptions we made concerning the ideal coupling, but mostly by the limitations of the PHD model. In a second time, the ACLR calculated with the ideal coupling seems to reach a limit (around -50dB) when the coupling gets lower and lower, whereas the ACLR calculated with the dynamic and real time solving model seems not limited. As before the most possible explanation is the limitations of the PHD to model PA non linearities, and thus the limit reached around -50dB is due to the limited accuracy of the model for PA non linearities.

In spite of these differences, it is significant to notice the shape of the three curves in figure 4.11 when the coupling raises significantly. It becomes a linear relation and the three curves tend to gather in a linear curve of factor almost 1 (0.978 for the curve concerning the distorted signal). The curve concerning the contribution from crosstalk only can be thus seen as an asymptotic limit for the ACLR, when the coupling raises. Indeed, the ACLR calculated from the crosstalk contribution has not been affected by any DPD and it contains no other PA non linearities, whereas the two other calculated ACLR do. Thus, it can be seen as the best ACLR achievable for a fixed coupling, which is the definition of a limit. From these comparisons between different calculated ACLR we can deduce that the -45dB limit for ACLR for WCDMA transmitters (appendix A.5.3) is reached in the best case for the presented PA models at a coupling factor of -11.6dB due to crosstalk effect.

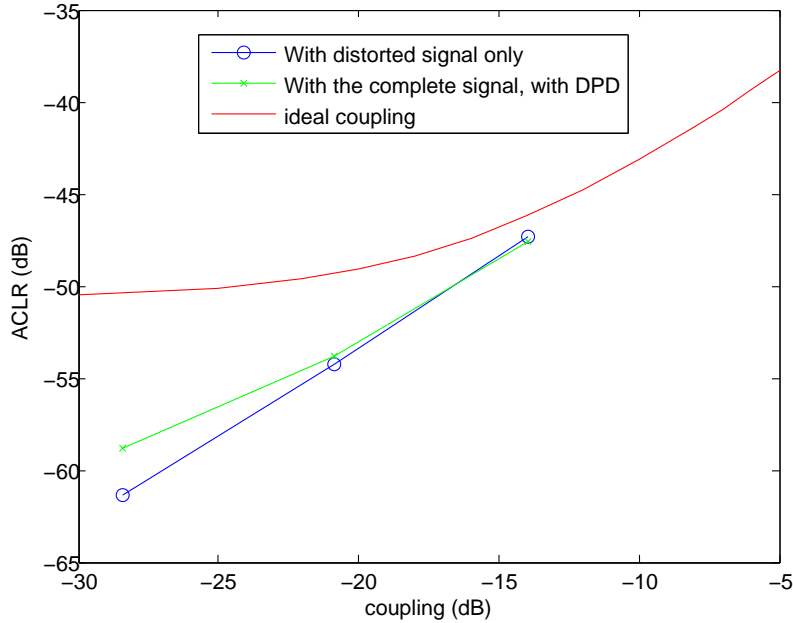


Figure 4.11: ACLR calculated in function of the coupling S_{12} for different output signals (blue: distorted signal only for dynamic model of the MIMO; green: complete signal for dynamic model of the MIMO; red: ideal coupling for time delayed MIMO)

4.4 Distortion of the radiated field

In all the previous sections the distortion has been analysed for the output wave of the PA, B_2 . However, to observe during measurements the distorted signal emitted by the antenna, it will be necessary to calculate the far field emitted by the antennas. The far field of the antenna is a product between an excitation factor $A(t)$ and a radiation function $E(\theta, \phi)$:

$$E_{emitted}(\theta, \phi) = A(t)E(\theta, \phi) \quad (4.13)$$

$A(t)$ is the amplitude and phase excitation and $E(\theta, \phi)$ is the unit far field function of the antenna. So for a single branch of the MIMO transmitter, we can write

$$E_{emitted,1}(\theta, \phi) = V_1(t)E_1(\theta, \phi) \quad (4.14)$$

where $V_1(t) = B_{2,1}(t) + A_{2,1}(t)$ is the voltage defined at the input of the antenna, and is thus the sum of the voltage waves $B_{2,1}(t)$ and $A_{2,1}(t)$. Applying the principle of superposition ([10] p390) in (4.14) for both branches of the MIMO transmitters, we can calculate the total E-field emitted from the transmitter:

$$E_{emitted,tot}(\theta, \phi) = V_1(t)E_1(\theta, \phi) + V_2(t)E_2(\theta, \phi) \quad (4.15)$$

where $E_1(\theta, \phi)$ and $E_2(\theta, \phi)$ are the far field unit functions of the two antennas, calculated one by one when the other is present but not excited. The unit far field functions are available in ADS Momentum. They are expressed as two functions, $E_\theta(\theta, \phi)$ and $E_\phi(\theta, \phi)$, which are the values of $E(\theta, \phi)$ in the space based on the unit spherical coordinate vectors $\hat{\theta}$ and $\hat{\phi}$. In a future measurement set-up, we will place one transmitter and one receiver in front of each other, such as the z-axis of the antennas will be parallel to each other. So the receiving plane of the antenna will be the E-plane, which is determined by the vectors \hat{r} and $\hat{\theta}$. Therefore, the received E field will be independent of the vector $\hat{\phi}$, and it is thus non relevant to observe the field $E_{tot,\phi}$. That's why the next plots and calculus will only depend on $E_{tot,\theta}$. In figures 4.12 is plotted the ACLR of $E_{tot,\theta}$ as function of ϕ and θ . We can first see that the ACLR is almost constant. The only variations are due to the variation of far field when the angle θ becomes too big: the directivity is indeed decreasing significantly when θ increases, and thus almost no E-field is radiated any more. Assuming that the receiving and emitted antennas are almost aligned, the angle θ will be low enough to consider the ACLR as constant in the measurement, and thus the distortion is independent on the positions of the antennas. It is nevertheless important to notice that the radiated power is still different for different orientations of the antennas.

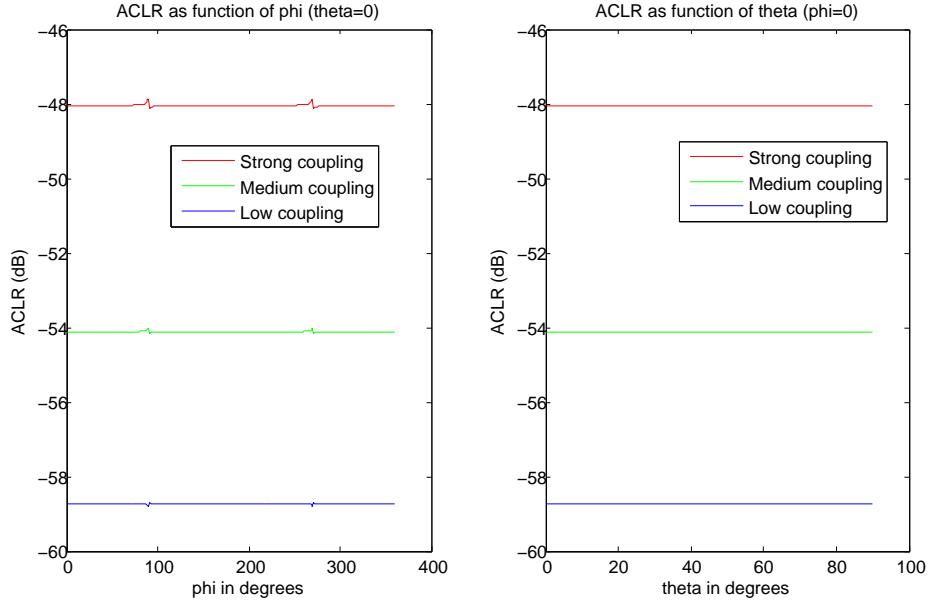


Figure 4.12: ACLR of the radiated $E_{tot,\theta}$ field in function of the angles θ (for $\phi = 0^\circ$) and ϕ (for $\theta = 0^\circ$)

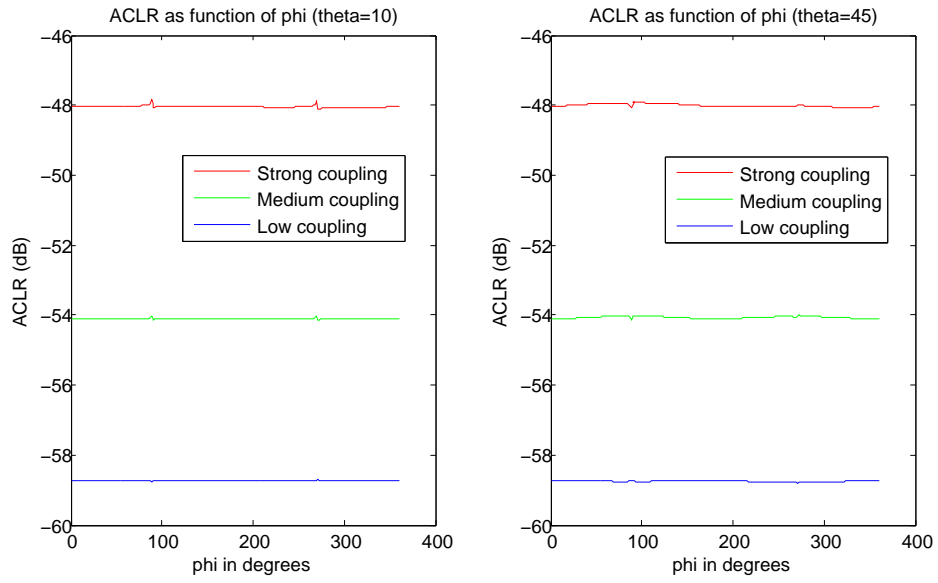


Figure 4.13: ACLR of the radiated $E_{tot,\theta}$ field in function of ϕ for $\theta = 10^\circ$ and $\theta = 45^\circ$

5 Experimental results

5.1 Measurement set up

In the aim to confirm the results obtained through simulations on MATLAB, measurements are required. The main purpose of the measurements is to calculate the ACLR of the output signal of a 2×2 MIMO transmitter. The measurement system described below is sketched in figures 5.1 and 5.2.

Whereas in the simulations the best ACLR achievable was found looking at the distortion generated by crosstalk only, it is impossible to reproduce in real measurements. Indeed the crosstalk contribution to distortion cannot be distinguished from the distortion due to the PA non-linearities. Therefore a good DPD is needed to linearise the PA present in the MIMO transmitter. A vector switched generalised memory polynomial (VSGMP) DPD [11] is used to linearise the PA.

The 2×2 MIMO transmitter is formed by two branches, each including a PA (both are CGH40006P from CREE in the test board CGH40006P-TB) linked to one antenna of one of the two elements antenna arrays previously designed. A dual-output high frequency arbitrary waveform generator (AWG) will be used to generate the IQ modulated RF signal for the two branches and a pre amplifier will be installed between the AWG and the PA for each branch of the MIMO in order to obtain a sufficient output power.

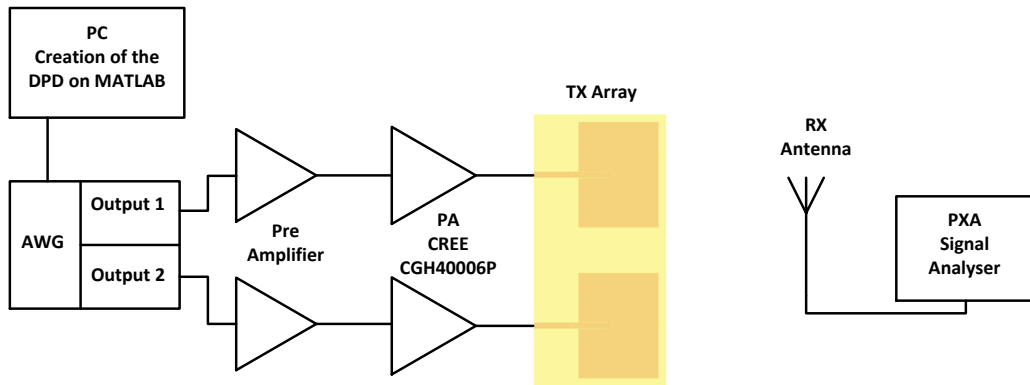


Figure 5.1: Diagram of the measurement system

The receiver consists of a single micro strip antenna linked by an SMA cable to an Agilent PXA vector signal analyser. For a simpler set up, the receive (RX) microstrip antenna will have the same dimensions and performance as the transmit (TX) antennas. Nevertheless, only a single port antenna is used and not an array like in the transmitter. The received signal will be analysed by the PXA via a MATLAB program to obtain the ACLR of the received signal. As aforementioned in section 4.4, the E-field emitted by the antenna array is independent from the angles θ and ϕ , and thus the disposition of the TX and RX antennas doesn't affect the ACLR of the signal. Nevertheless the TX and RX antennas will be placed in line of sight of each other to avoid unnecessary losses due to the antenna far field radiation pattern or due to different propagation paths. The TX and RX antennas have thus a common E-plane.

In a matter of coherence with the performed simulations, the WCDMA signal used for the measurements is the signal used during simulations emitted at 2.12GHz. It will be pre distorted using the VSGMP algorithm in MATLAB before being sent through the AWG and then to the MIMO transmitter. It is important to notice that the signals sent in each branch of the transmitter are independent from each other and correspond each to a half of the WCDMA signal.

Concerning the determination of the coefficients which characterise the VSGMP DPD, they are calculated for each branch of the MIMO transmitter and thus for each PA, but with both PAs biased. This determination of the coefficients of the DPD is thus closer to the real conditions of the MIMO signal transmission. Some iterations in the DPD are necessary for each PA and the coefficients are chosen to obtain the best ACLR for the signal received at the RX antenna when only the considered branch is transmitting.

Pictures of the MIMO transmitter and the receiving antenna are available in appendix D.

Once both branches of the MIMO transmitter have been linearised, the pre distorted signals can be transmitted and received through the PXA signal analyser.

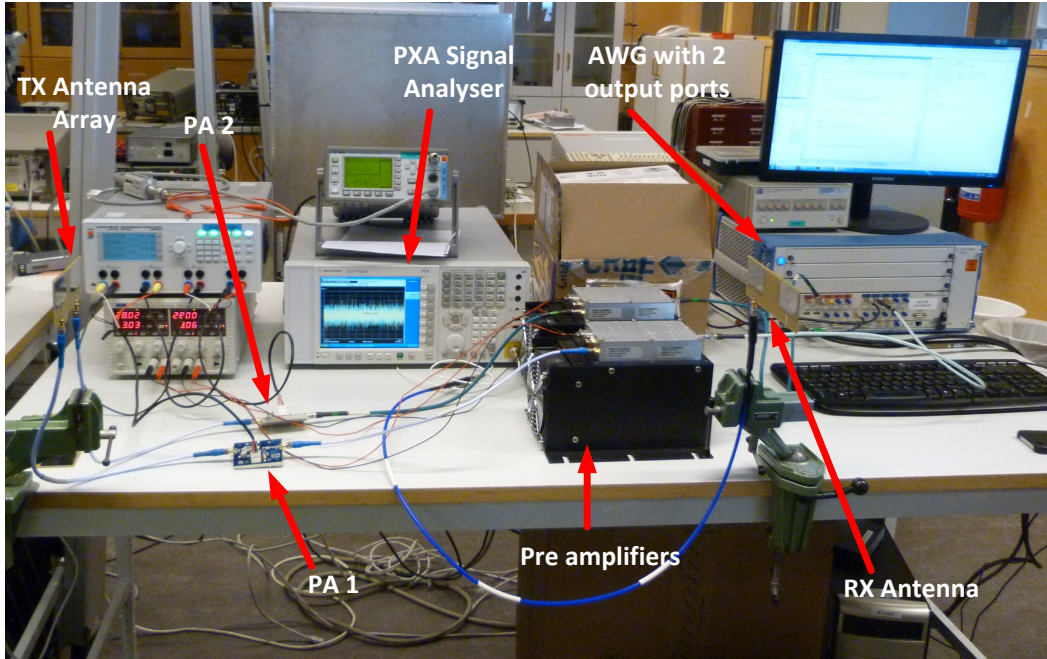


Figure 5.2: Picture of the measurement system with legend

5.2 Measurement results

The measurement has been repeated for the three different array designs: for low, medium and high coupling between the micro strip antennas. The output spectrum is measured from the PXA and plotted in figure 5.3 for the three different antenna arrays as TX antenna.

The first statement we can make is that the measurements confirm the results observed in the simulations: crosstalk leads to signal distortion through spectral regrowth. In particular the ACLR will be affected as we can see in figure 5.4, detail of the figure 5.3. The results are summarized in the table 5.1 below.

Table 5.1: ACLR measured for the different arrays

	Measured S_{12} (dB) at 2.12GHz	ACLR (dB)		
		only 1 branch transmitting	both branches transmitting	ACLR degradation
d1	-13.98	-58.99	-46.36	12.63
d2	-20.86	-58.75	-52.27	6.48
d3	-28.39	-59.60	-57.36	2.24

The DPD used in the measurements linearises the PA enough so that the worsening in ACLR observed (last column in the table) can be considered as mainly due to crosstalk effect. Indeed each PA has been linearised to obtain an ACLR at least equal to the ACLR mentioned in the third column of table 5.1 (named "only 1 branch transmitting"), which is better than the measured ACLR when both branches are transmitting. Moreover, comparing the measured ACLR and the theoretical best achievable ACLR displayed in table 4.1, we can say that the measurements are very close to the results of the MIMO simulations, in particular for high and medium coupling (see figure 5.5). Indeed the DPD is still limited to linearise the PA and so the difference is bigger when the distortion due to crosstalk becomes less significant than the remaining distortion due to the non-linearities of the PA. It also confirms the previous idea which states that the theoretical ACLR calculated in table 4.1 can be

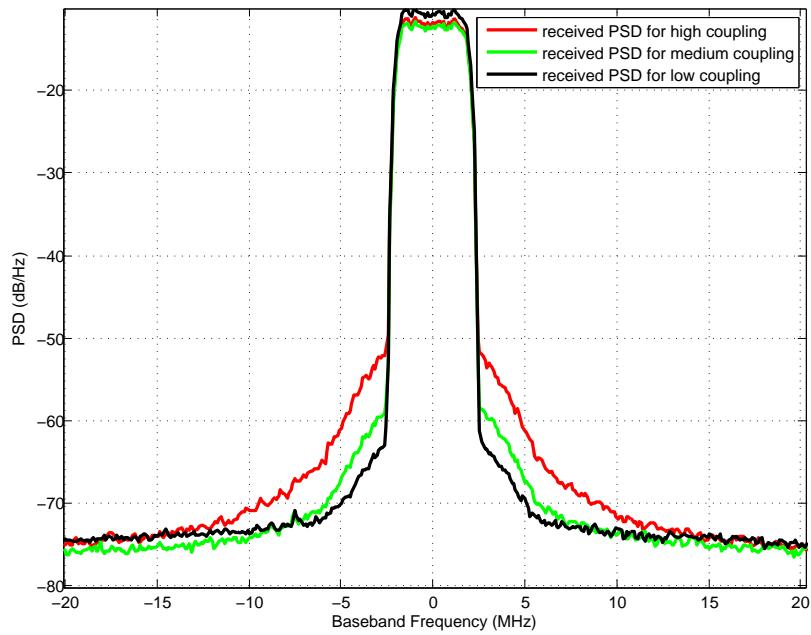


Figure 5.3: Power Spectral Density of the received signal for the three different antenna arrays (in red: high coupling; in green: medium coupling; in black: low coupling)

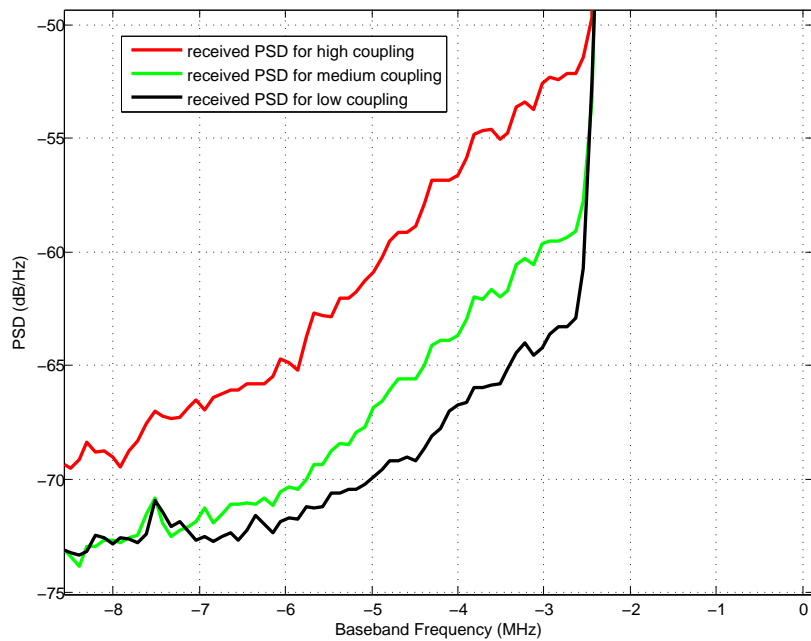


Figure 5.4: Detail of figure 5.3: zoom on the lower part of the main channel and on the first adjacent channel

seen as the best achievable ACLR, calculated when the DPD compensates perfectly the non linearities of the PA.

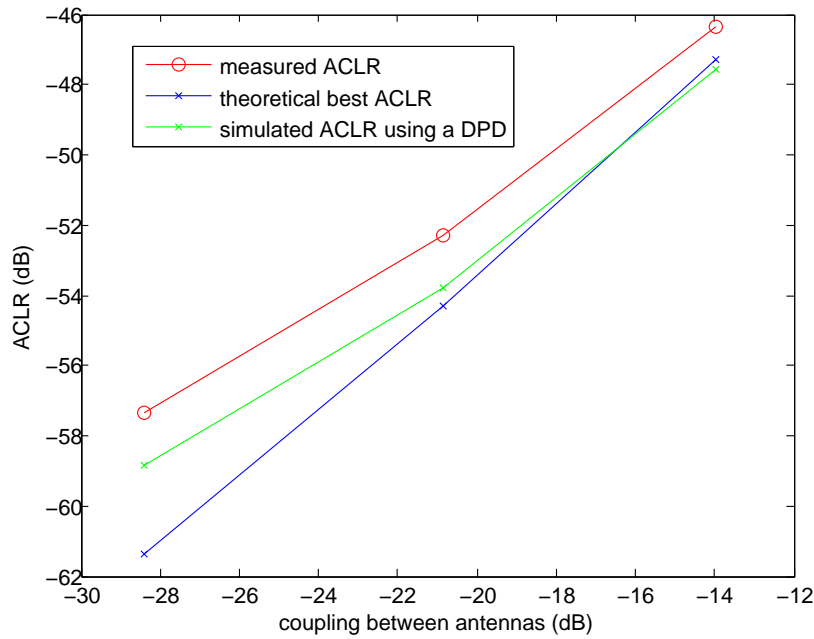


Figure 5.5: measured ACLR values, theoretical best achievable ACLR and simulated ACLR (complete signal with a DPD) in function of the coupling between antennas

According to the results of the measurement the deterioration in ACLR seems linear in dB, as we have witnessed in the simulations. In figure 5.6 the deterioration of the ACLR versus the coupling of the antenna array is outlined. Even though more measurements with different coupling between antennas would be a significant improvement to confirm this fact, the deterioration of the ACLR appears to increase linearly in dB with the coupling.

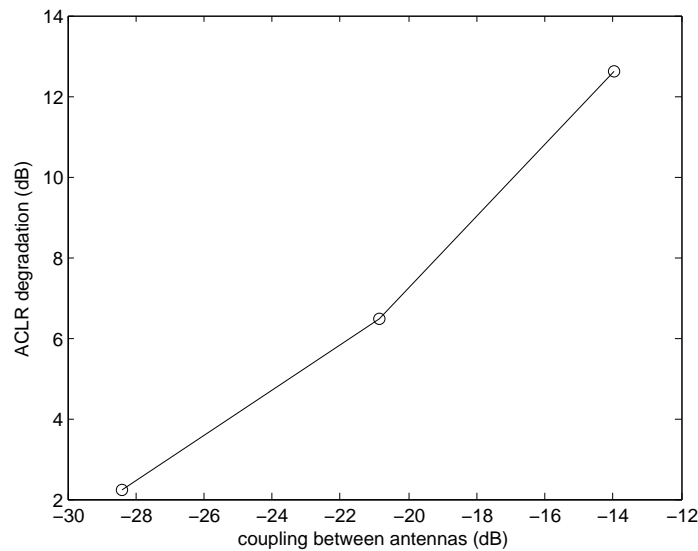


Figure 5.6: Measured deterioration of the ACLR as function of the coupling between the antennas (the reference ACLR is the ACLR calculated when only one branch of the MIMO is transmitting)

If we consider that the ACLR is increasing linearly with the coupling, the -45dB limit in ACLR for 3G transmitters (see appendix A.5.3) can be reached for a coupling of -12.4dB between the antennas.

6 Conclusions

6.1 Results from present work

In this thesis the contribution of crosstalk to signal distortion in a MIMO transmitter has been analysed by two different methods: simulations and measurements.

Because most existing behavioral models consider only one input, two new models have been developed to simulate the output of the PA in conditions of crosstalk. First a static model based on the polyharmonic distortion model [8] gives us a rough idea of the crosstalk effect on the signal distortion for CW signals. To simulate modulated signals like WCDMA, a dynamic model has been developed based on a dual-input complex memory polynomial and this model has proven to be very accurate. Using this newly developed model, it was thus possible to simulate a complete 2×2 MIMO transmitter and then observe the signal distortion resulting from crosstalk, in terms of spectral regrowth and ACLR. A theoretical limit for the ACLR in crosstalk conditions has been highlighted, determining a best achievable ACLR for the output signal and for a given coupling between the antennas of the transmitter.

To confirm the results found in simulations, measurements have been carried in collaboration with the Signals and Systems Department. Antenna arrays have been designed, based on micro strip antennas and for different coupling - determined by the distance between the patch centres. Using a DPD to linearise the PA, a MIMO transmitter was set up and the output spectrum of the transmitter was measured when both branches of the MIMO are emitting. The distortion of the signal has been thus measured calculated the ACLR in function of the coupling.

To conclude, we can say that the signal is considerably affected by crosstalk: the ACLR worsens almost linearly in dB with the increasing coupling between the antennas, and the -45 dB limit defined by 3GPP standards can be reached at -12.4 dB coupling. Although -12.4 dB coupling can be considered as a very high coupling, higher requirements in terms of signal distortion and ACLR are set by base stations constructors. In this way the distortion of the signal due to crosstalk effect cannot be neglected and isolators are still necessary for strong coupling antenna structures.

6.2 Future work

Beyond the analysis of PA output signal distortion due to crosstalk, these results may be a basis for further steps and projects.

Among these future steps, the simulation can be extended to greater MIMO systems, not 2×2 MIMO transmitters anymore but $N \times N$ MIMO transmitters. The idea is there to simulate a large and complete MIMO system, to observe the signal distortion depending on different parameters, such as crosstalk. In this case the developed dynamic model can be very useful and the MATLAB algorithm used to simulate the MIMO transmitter would need a few modifications.

Linearisation of the PA is always a significant step in the transmission of the signal to avoid unnecessary distortion. The previously developed dynamic model is useful in the way it includes two inputs, and so it can take the reflections from mismatch and the crosstalk effects into account. Developing a DPD based on this new PA behavioral model to compensate for reflections from mismatch and crosstalk effects may be one of the future steps in the creation of new DPDs for MIMO systems.

References

- [1] 3rd Generation Partnership Project (3GPP). *Technical Specification Group Radio Access Network; Base Station (BSS) Radio Transmission and Reception (FDD)*, Release 11. Available at www.3gpp.org/ftp/Specs/archive/25_series/25.104/25104-b50, March 2013.
- [2] C.A.Balanis. *Antenna Theory: Analysis and Design - 3rd Edition*. Wiley, Hoboken, NJ, 2005.
- [3] R. E. Collin. *Foundations for Microwave Engineering - 2nd Edition*. Wiley, Hoboken, NJ, 2001.
- [4] D.Schreurs et al. *RF Power Amplifier Behavioral Modeling*. Cambridge University Press, Cambridge, UK, 2009.
- [5] G.David et al. From Theory to Practice: An Overview of Space-Time coded Wireless Systems. *IEEE J. Sel Areas Commun.*, vol.21:pp.281–302, 2003.
- [6] G.Z.El Nashef et al. Behavioral Model of Solid State Power Amplifiers (SSPAs) for Agile Antennas Application. *Proc. 4th European Conf. Antennas and Propag. (EuCAP)*, pages 1–4, 2010.
- [7] H.Bölskei. MIMO-OFDM Wireless Systems: Basics, Perspectives and Challenges. *IEEE Wireless Commun.*, vol.13:pp.31–37, 2006.
- [8] J.Verspecht and D.E.Root. Polyharmonic Distortion Modeling. *IEEE Microwave*, vol.7:pp.44–57, 2006.
- [9] S.Gustafsson M.Thorsell and C.Fager. A novel active Load-Pull System with Multi-Band Capabilities. *Proc. 81st ARFTG Microwave Measurement Conf.*, 2013.
- [10] P.S.Kildal. *Foundations of Antennas: A Unified Approach for Line-Of-Sight and Multipath*. Compendium in Antenna Engineering at Chalmers, Göteborg, Sweden, 2009.
- [11] S.Afsardoost T.Eriksson and C.Fager. Digital Predistortion Using a Vector-Switched Model. *IEEE Trans. Microwave Theory Tech.*, vol.60:pp.1166–1174, 2012.
- [12] Fan Yang and Yahya Rahmat-Samii. Microstrip Antennas Integrated With Electromagnetic Band-Gap (EBG) Structures: A Low Mutual Coupling Design for Array Applications. *IEEE Trans. Antennas Propag.*, vol.51:pp.2936–2946, 2003.

List of Figures

1.1	Structure of a MIMO transmitter with N antennas, including circulators	1
1.2	Structure and Channel Matrix of a MxN MIMO	2
1.3	Spatial Multiplexing Gain in a MIMO	2
2.1	Gain compression of the PA for various gate voltages	6
2.2	Detailed gain compression for various gate voltages	7
2.3	PAE and gain of the device at $-2.71V$ voltage at the gate	7
2.4	Single tone load-pull system used to extract the output B_2 for various amplitude and phase of the input signals A_1 and A_2	10
2.5	Magnitude and phase of the scattering function S_{21}	11
2.6	Measured Gain (green curve) and gain simulated with the static model (red curve) . .	11
2.7	Magnitude and phase of the scattering function S_{22}	12
2.8	Magnitude and phase of the scattering function T_{22}	12
2.9	Active load-pull system and generated signals A_1 , A_2 and B_2 used to extract the coefficients of the dynamic model	15
2.10	NMSE in dB for the dynamic model, with $Q = 2$ and coefficients calculated with input signals of $24dBm$ and $26dBm$ maximum input power	16
2.11	NMSE in dB for the dynamic model in functions of the degree P and the number of considered delays Q , with fixed $L = 2$	17
2.12	NMSE in dB for the dynamic model in functions of the degree L and the number of considered delays Q , with fixed $P = 4$	17
2.13	ACEPR in function of the maximum peak power of the multi-sine input signal A_1 . Calculated over all the measurements with $P = 4$, $L = 2$ and $Q = 2$	18
2.14	NMSE in dB for the Static model, calculated over the data series of the dynamic model extraction (here the static model is extracted through a spline using MATLAB)	19
2.15	DPD within the transmitter architecture	19
2.16	Effect of the DPD on the spectrum of the output signal of the PA, considering a WCDMA signal at the input	20
2.17	Indirect learning method to design the dynamic DPD	21
3.1	Antenna layout, physical and electrical length	23
3.2	Two slots model for a transmission line (Y_c is the line impedance)	24
3.3	New design of the antenna including the inset feed line	25
3.4	Dimensions of the designed antenna layout	26
3.5	Simulated radiation pattern of one of the arrays (medium coupling, 0.429λ between patch centres)	27
3.6	Manufactured antenna arrays: 3 different designs for 3 different coupling values	27
3.7	Measured S11 for the three designs. Red for strong coupling, green for medium coupling and blue for low coupling	28
3.8	Measured S12 for the three designs. Red for strong coupling, green for medium coupling and blue for low coupling	29
4.1	Description of ideal coupling for a 2×2 MIMO transmitter with a coupling factor $\alpha_{coupling}$ between the two branches	31
4.2	Spectrum of the signal on the two channels (channel 1 on the left, channel 2 on the right) of the MIMO transmitter, with DPD (in blue) and without a DPD (in red). Spectrum of the input signal is displayed in blue. A coupling factor of $-14dB$ between the antennas has been used	32
4.3	Simulated ACLR for the output of a MIMO channel under condition of crosstalk. In red, the $-45dB$ limit for WCDMA communication systems	33
4.4	MIMO model representation: solving the $B_{2,i}$ as unknowns of a system of equations . .	34
4.5	Spectrum of the output and input signals from the MIMO transmitter without DPD (on the left: branch 1; on the right: branch 2)	36
4.6	Spectrum of the output signal for different array designs (red:strong coupling; green: medium coupling; black:low coupling) and spectrum of the input signal after the DPD	37
4.7	Spectrum of the output signal coming only from crosstalk for different array designs (red:strong coupling; green: medium coupling; black:low coupling)	37

4.8	Comparison of the output spectrum considering the complete signal and using a DPD (straight lines) and the contribution from crosstalk (dashed lines) for different array design (red:strong coupling; green: medium coupling; black:low coupling)	38
4.9	Detail of figure 4.8 showing the spectrum on the lower adjacent channel channel (from -2.5MHz to -7.5MHz)	39
4.10	ACLR as function of the coupling S_{12} between the antennas	39
4.11	ACLR calculated in function of the coupling S_{12} for different output signals (blue: distorted signal only for dynamic model of the MIMO; green: complete signal for dynamic model of the MIMO; red: ideal coupling for time delayed MIMO)	40
4.12	ACLR of the radiated $E_{tot,\theta}$ field in function of the angles θ (for $\phi = 0^\circ$) and ϕ (for $\theta = 0^\circ$)	41
4.13	ACLR of the radiated $E_{tot,\theta}$ field in function of ϕ for $\theta = 10^\circ$ and $\theta = 45^\circ$	42
5.1	Diagram of the measurement system	43
5.2	Picture of the measurement system with legend	44
5.3	Power Spectral Density of the received signal for the three different antenna arrays (in red: high coupling; in green: medium coupling; in black: low coupling)	45
5.4	Detail of figure 5.3: zoom on the lower part of the main channel and on the first adjacent channel	45
5.5	measured ACLR values, theoretical best achievable ACLR and simulated ACLR (complete signal with a DPD) in function of the coupling between antennas	46
5.6	Measured deterioration of the ACLR as function of the coupling between the antennas (the reference ACLR is the ACLR calculated when only one branch of the MIMO is transmitting)	46
A.1	Incident and scattered voltage waves in a 2-port network	53
A.2	Transmitter of a $N \times N$ MIMO with the different voltage waves $A_{1,i}$, $A_{2,i}$ and $B_{2,i}$ for the different branches	54
A.3	Power spectral density of a WCDMA signal centered at 2.14GHz with the main channel signal bandwidth and the adjacent channel signal bandwidth, each being 3.84MHz wide	55
C.1	Layout on the software ADS of the antenna array designed to provide a medium coupling (distance to centres is 0.429λ)	58
C.2	Layout in ADS sent to Sunstone circuits and including the three antenna arrays	59
C.3	Absolute E field in the E-plane in function of θ in dB and in Volt	60
C.4	Absolute E field in the H-plane in function of θ in dB and in Volt	60
D.1	Picture of the MIMO transmitter including the antenna array and the PAs	61
D.2	Picture of the receiving antenna used in the measurement	62

List of Tables

3.1	Coupling between the different array designs	28
4.1	ACLR between the different array designs	38
5.1	ACLR measured for the different arrays	44

A Useful definitions

A.1 2-port network, reflection coefficient

The amplifier is in this project considered as a 2-port device. Even though in our case we cannot consider the PA like a linear device, the easiest and most convenient way to describe a linear two port device is S-parameters. The S-parameters are a way to describe the behavior of the device by expressing the incident and scattered voltage waves in function of each other.

$$S_{ij} = \frac{V_i^-}{V_j^+}, V_k^+ = 0, \text{ for } k \neq j \quad (\text{A.1})$$



Figure A.1: Incident and scattered voltage waves in a 2-port network

The S-parameters define thus a S-matrix for the network:

$$\begin{pmatrix} V_1^- \\ V_2^- \end{pmatrix} = \begin{pmatrix} S_{11} & S_{12} \\ S_{21} & S_{22} \end{pmatrix} \begin{pmatrix} V_1^+ \\ V_2^+ \end{pmatrix} \quad (\text{A.2})$$

The scalar gain of this 2-port network is thus $G = |S_{21}|$ and the input voltage reflection coefficient is defined as $\Gamma = S_{11}$ if the 2-port network is matched to the connected load.

A.2 Reflected and incident voltage waves

In this thesis we will consider the reflected and incident voltage waves as defined below. The incident voltage waves are named A_1 for port 1 and A_2 for port 2, and the reflected voltage waves are named B_1 and B_2 .

$$\begin{pmatrix} B_1 \\ B_2 \end{pmatrix} = \begin{pmatrix} S_{11} & S_{12} \\ S_{21} & S_{22} \end{pmatrix} \begin{pmatrix} A_1 \\ A_2 \end{pmatrix} \quad (\text{A.3})$$

The scalar input (or output) power on a port of this two port network can be thus defined as

$$P_{A_i} = \frac{A_i^2}{2Z_{ref}} \quad (\text{A.4})$$

where Z_{ref} is the reference impedance at the input of the two port network.

A.3 IQ Data

Different techniques are used to modulate RF signals. A modulated signal can be expressed as:

$$\begin{aligned} s(t) &= \Re\{A(t)e^{j\phi(t)}e^{2\pi j f_c t}\} \\ &= \Re\{(A(t)\cos(\phi(t)) + jA(t)\sin(\phi(t)))e^{2\pi j f_c t}\} \\ &= \Re\{(I(t) + jQ(t))e^{2\pi j f_c t}\} \end{aligned} \quad (\text{A.5})$$

where f_c is the carrier frequency and $\Re\{x\}$ is the real part of x . I stands for In-phase and Q stands for Quadrature phase. The modulated signal can be thus seen as a complex baseband signal $I(t) + jQ(t)$, result of the combination of the real signals I and Q.

A.4 Notations in this thesis

In this thesis, we will use the following notations.

As seen previously in A.2, the incident voltage waves A_1 and A_2 are the ordinary incident voltage wave and the back-coming incident voltage wave (usually seen as the secondary input), respectively. B_2 is therefore the scattered voltage wave.

In the case of a transmitter in a $N \times N$ MIMO, $A_{1,i}$, $A_{2,i}$ and $B_{2,i}$ are the ordinary incident voltage wave, the back-coming incident voltage wave and the scattered voltage wave of the i^{th} branch of the transmitter, respectively. This notation is described in figure A.2.

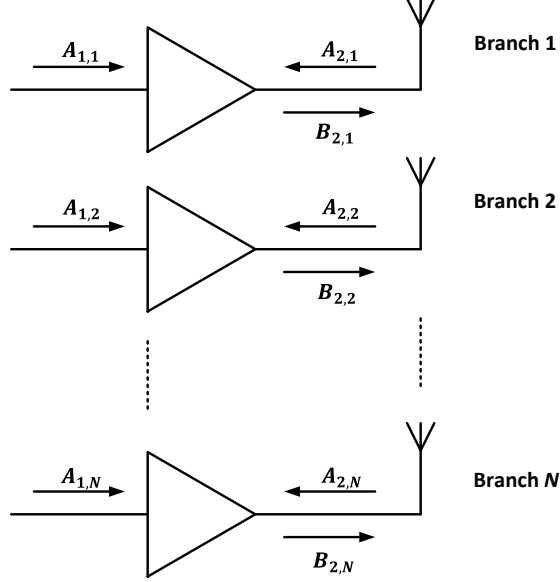


Figure A.2: Transmitter of a $N \times N$ MIMO with the different voltage waves $A_{1,i}$, $A_{2,i}$ and $B_{2,i}$ for the different branches

A.5 Mathematical tools and functions

A.5.1 Least Squares Method

The Least Squares method (LSM) is a method developed to determine a group of unknowns using many equations. It is particularly suited to solve systems of linear equations.

Systems of linear equations can be written as $y = \sum_{i=1}^N \theta_i h_i$, where h_i are the variables and θ_i are the unknown parameters to be determined. Considering a linear system $S_{y,H,\theta}$ of M equations and N unknowns with M greater than N , where \mathbf{y} is a column vector of M rows, \mathbf{H} is a $M \times N$ matrix and $\boldsymbol{\theta}$ is a column vector of N rows. The system $S_{y,H,\theta}$, can be expressed as:

$$\mathbf{y} = \mathbf{H}\boldsymbol{\theta} \quad (\text{A.6})$$

The aim of the linear LSM is to minimize the squared error between the data measurement and the estimated parameters $\hat{\boldsymbol{\theta}}$, that means obtaining the minimum of the function $f(\hat{\boldsymbol{\theta}}) = \|\mathbf{y} - \mathbf{H}\hat{\boldsymbol{\theta}}\|^2$. In a computational point of view, the solution is determined by:

$$\hat{\boldsymbol{\theta}} = (\mathbf{H}^T \mathbf{H})^{-1} \mathbf{H}^T \mathbf{y} = \mathbf{H}^+ \mathbf{y} \quad (\text{A.7})$$

Where \mathbf{H}^+ is the pseudo inverse matrix of \mathbf{H} . In MATLAB, this method is used to calculate unknown parameters through the command $\hat{\boldsymbol{\theta}} = \mathbf{H} \backslash \mathbf{y}$.

A.5.2 Mean Squared Error (NMSE)

The normalized mean squared error (NMSE) can be seen as an estimation of the expected error between a data measurement and a simulated value aimed to reproduce this measurement. The lower the NMSE

is, the more accurate the simulation is. In our case it will be useful to compare the different models and compare their accuracy. If \mathbf{y}_{meas} are the measured values and \mathbf{y}_{sim} are the simulated values, the NMSE can be described as the ratio between the variance of the error between the real and simulated values and the variance of the real measurement data:

$$NMSE(\mathbf{y}_{\text{meas}}, \mathbf{y}_{\text{sim}}) = \frac{\text{var}(\mathbf{y}_{\text{meas}} - \mathbf{y}_{\text{sim}})}{\text{var}(\mathbf{y}_{\text{meas}})} \quad (\text{A.8})$$

A.5.3 Channel Leakage Ratio

The adjacent leakage ratio (ACLR) is the ratio between the power of a signal emitted in the signal bandwidth of the adjacent channel and the power of the same signal emitted in the signal bandwidth of the main channel. It can be seen as the ratio between the intermodulation signal and the useful signal. The signal bandwidth is different from the channel bandwidth, as it is within the latter. In WCDMA signals, the signal bandwidth is typically 3.84MHz and the channel bandwidth is 5MHz which allows a signal channel separation of 1.16MHz. Usually, ACLR is used for WCDMA signals whereas ACPR (adjacent channel power ratio) is used for IS-95⁵ signals and so only used for 2G signals. In this thesis, we will consider the ratio as negative, $ACLR_{dB} \leq 0$.

$$ACLR_{dB} = 10 \times \log\left(\frac{\int_{adj\ ch} |Y(f)|^2 df}{\int_{main\ ch} |Y(f)|^2 df}\right) [4] \quad (\text{A.9})$$

where $Y(f)$ is the Fourier transform of the signal, *adj ch* and *main ch* represent the signal bandwidth of the adjacent channel and the signal bandwidth of the main channel.

In figure A.3, it corresponds to the ratio between the spectral power contained in the adjacent channel signal bandwidth (green area) and the spectral power contained in the main channel signal bandwidth (blue area). Notice that the signal plotted here is a WCDMA signal, with a main channel signal bandwidth of 3.84MHz in total.

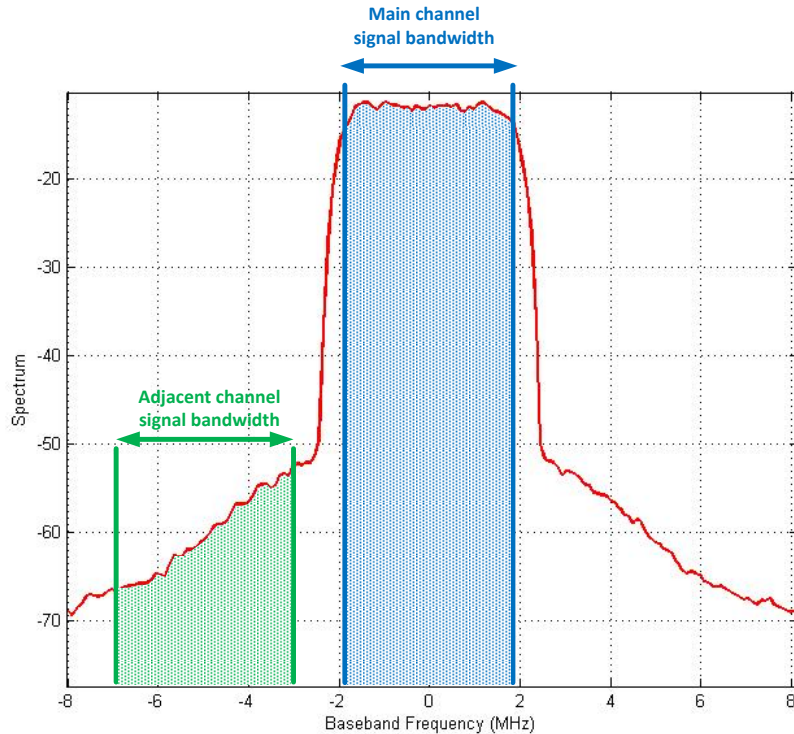


Figure A.3: Power spectral density of a WCDMA signal centered at 2.14GHz with the main channel signal bandwidth and the adjacent channel signal bandwidth, each being 3.84MHz wide

⁵IS-95 is a CDMA protocol defined by Qualcomm

It is also possible to calculate the adjacent channel error power ratio (ACEPR) which is the ratio between the error power (error between a measurement and a simulation) of the signal in the adjacent channel and the power in the main band channel [4].

$$ACEPR = 10 \times \log\left(\frac{\int_{adj\ ch} |Y_{measured}(f) - Y_{simulated}(f)|^2 df}{\int_{main\ ch} |Y_{measured}(f)|^2 df}\right) \quad (A.10)$$

It is significant to note that the maximum limit for ACLR in WCDMA and LTE communication systems is fixed at -45dB [1]. To achieve this requirement, the ACLR of the output signal of the transmitter must be better than -45dB .

B Dynamic non linear model matrices equation

This appendix details the matrix form in (2.24) which is the main equation of the dynamic polynomial model for the PA. (2.24) is recalled below:

$$\mathbf{B}_2 = \mathbf{H}(A_1, A_2)\boldsymbol{\theta}$$

In (2.24), $\boldsymbol{\theta}$ corresponds to the coefficients of the model and are meant to be extracted. A_1 , A_2 and B_2 are the incident voltage waves and the measured scattered voltage wave, respectively, and they are expressed in time domain.

K corresponds to the number of rows in the matrices. K is therefore bigger than the number of coefficients M and $t + KT$ is smaller than the record length.

\mathbf{B}_2 , $\boldsymbol{\theta}$ and $\mathbf{H}(A_1, A_2)$ are described below:

$$\mathbf{B}_2 = \begin{bmatrix} B_2(t) \\ B_2(t+T) \\ \vdots \\ B_2(t+KT) \end{bmatrix} \quad (\text{B.1})$$

$$\boldsymbol{\theta} = \begin{bmatrix} \theta_1 \\ \theta_2 \\ \vdots \\ \theta_M \end{bmatrix} \quad (\text{B.2})$$

where $M = LQ^2 + (P + 2L)Q + P + L$.

$$\mathbf{H}(\mathbf{A}_1, \mathbf{A}_2) = \begin{bmatrix} \mathbf{H}_1[A_1(t)] & \mathbf{H}_2[A_1(t), A_2(t)] & \mathbf{H}_3[A_1(t), A_2^*(t)] \\ \mathbf{H}_1[A_1(t+T)] & \mathbf{H}_2[A_1(t+T), A_2(t+T)] & \mathbf{H}_3[A_1(t+T), A_2^*(t+T)] \\ \vdots & \vdots & \vdots \\ \mathbf{H}_1[A_1(t+KT)] & \mathbf{H}_2[A_1(t+KT), A_2(t+KT)] & \mathbf{H}_3[A_1(t+KT), A_2^*(t+KT)] \end{bmatrix} \quad (\text{B.3})$$

where $\mathbf{H}_1[A_1(t)]$, $\mathbf{H}_2[A_1(t), A_2(t)]$ and $\mathbf{H}_3[A_1(t), A_2^*(t)]$ are respectively defined by:

$$\mathbf{H}_1[A_1(t)] = [A_1(t) \cdots A_1(t - Q\Delta) \cdots A_1(t) | A_1(t) |^{2i} \cdots A_1(t - Q\Delta) | A_1(t - Q\Delta) |^{2i} \cdots A_1(t - Q\Delta) | A_1(t - Q\Delta) |^{2P}] \quad (\text{B.4})$$

$$\mathbf{H}_2[A_1(t), A_2(t)] = [A_2(t) \cdots A_2(t - Q\Delta) \cdots A_2(t) | A_1(t) |^{2i} \cdots A_2(t - Q\Delta) | A_1(t) |^{2i} \cdots A_2(t) | A_1(t - Q\Delta) |^{2i} \cdots A_2(t - Q\Delta) | A_1(t - Q\Delta) |^{2L}] \quad (\text{B.5})$$

$$\mathbf{H}_3[A_1(t), A_2^*(t)] = A_2^*(t) A_1^2(t) \cdots A_2^*(t - Q\Delta) A_1^2(t) \cdots A_2^*(t) A_1^2(t - Q\Delta) \cdots A_2^*(t - Q\Delta) A_1^2(t - Q\Delta) \cdots A_2^*(t) A_1^2(t) | A_1(t) |^{2j} \cdots A_2^*(t - Q\Delta) A_1^2(t - Q\Delta) | A_1(t - Q\Delta) |^{2(L-1)} \quad (\text{B.6})$$

C Antenna Layout and Radiation Fields

In this Appendix is presented the antenna layout on ADS for a single transmitter and the layout sent to Sunstone Circuits ⁶. Some radiation fields are also provided.

C.1 Antenna layout in ADS

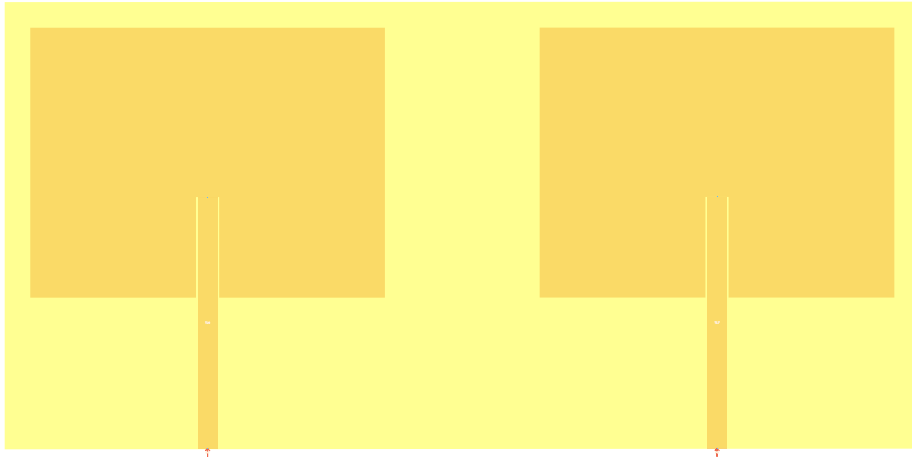


Figure C.1: Layout on the software ADS of the antenna array designed to provide a medium coupling (distance to centres is 0.429λ)

⁶<http://www.sunstone.com/QuoteQT.aspx>

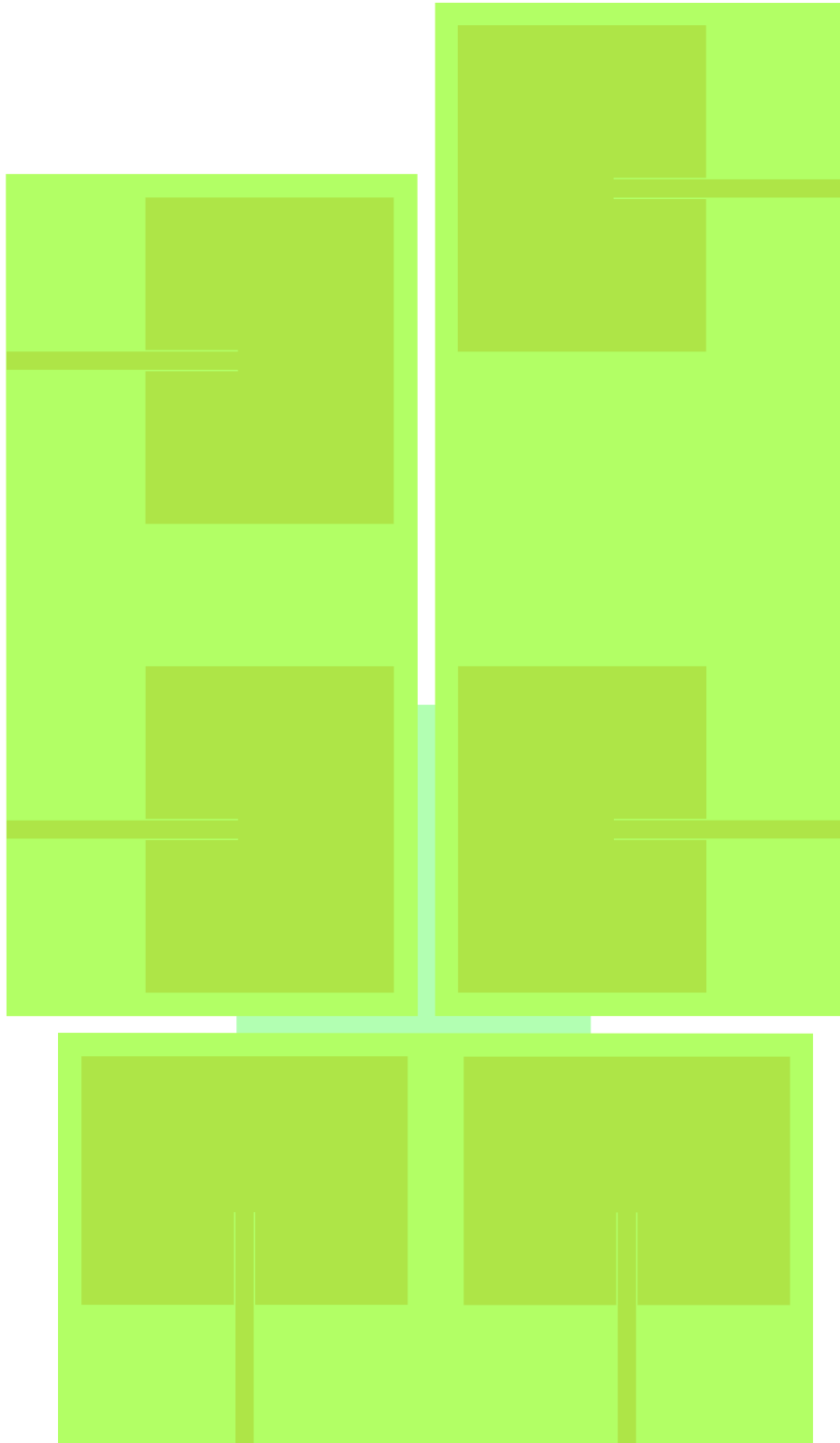


Figure C.2: Layout in ADS sent to Sunstone circuits and including the three antenna arrays

C.2 Radiation Fields

The E plane of the micro strip antenna is the plane xz , where z is the vector perpendicular to the patch plane and x is the vector parallel to the direction of the inset feed. The H-plane is thus the plane yz perpendicular to the E-plane. Below are presented the absolute E-field emitted by the two-antennas array with a distance between antennas centres of 0.429λ , i.e. medium coupling, for a frequency of 2.167GHz. E_θ is the value of the E-field in the direction of $\hat{\theta}$ and E_ϕ is the value of the E-field in the direction of $\hat{\phi}$. These values have been obtained using the software ADS Momentum from Agilent.

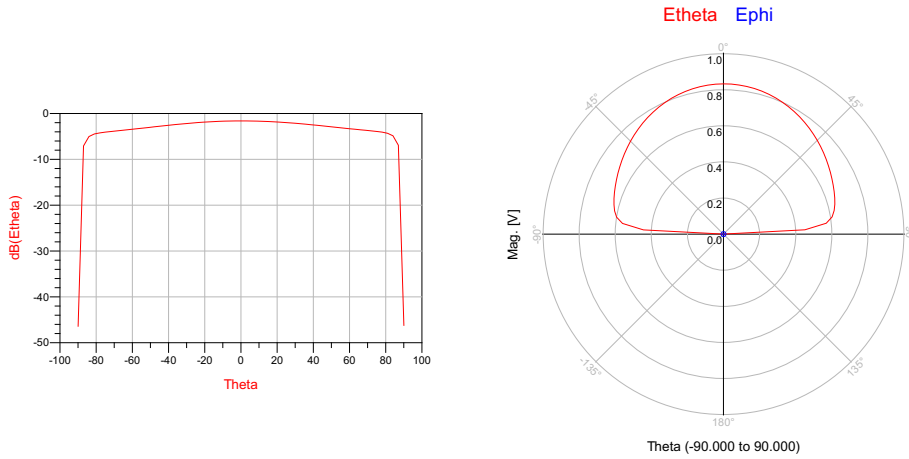


Figure C.3: Absolute E field in the E-plane in function of θ in dB and in Volt

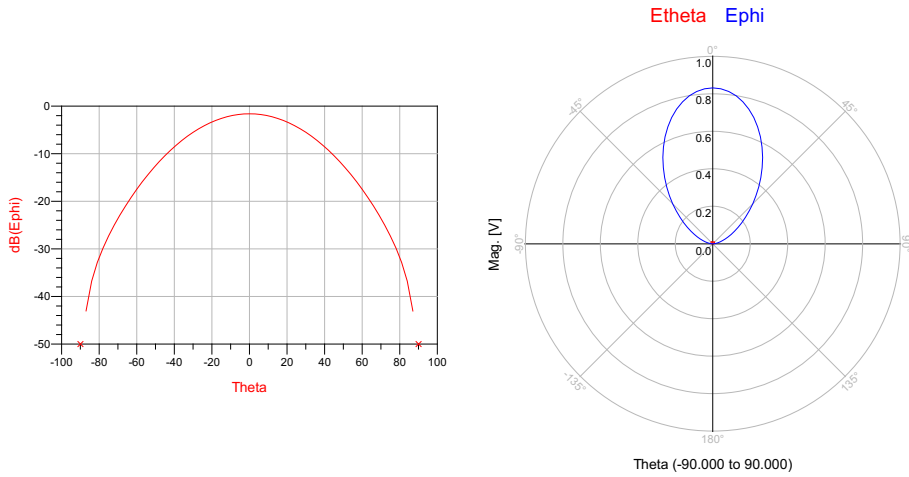


Figure C.4: Absolute E field in the H-plane in function of θ in dB and in Volt

D Measurement Set Up

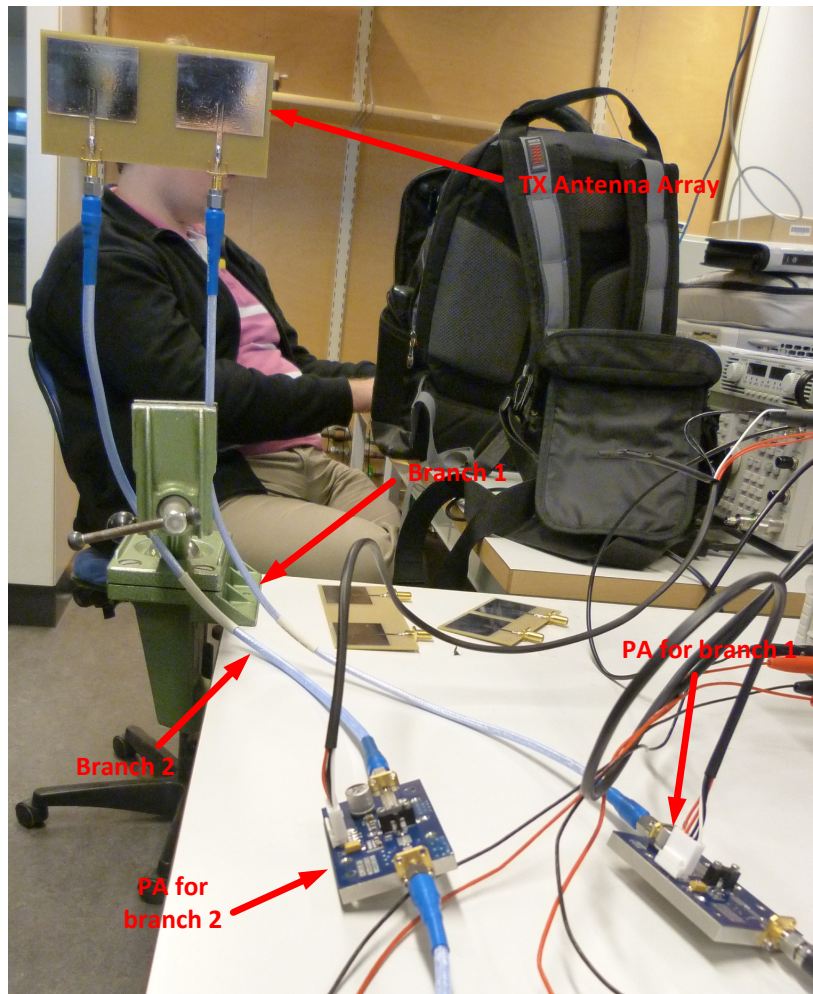


Figure D.1: Picture of the MIMO transmitter including the antenna array and the PAs

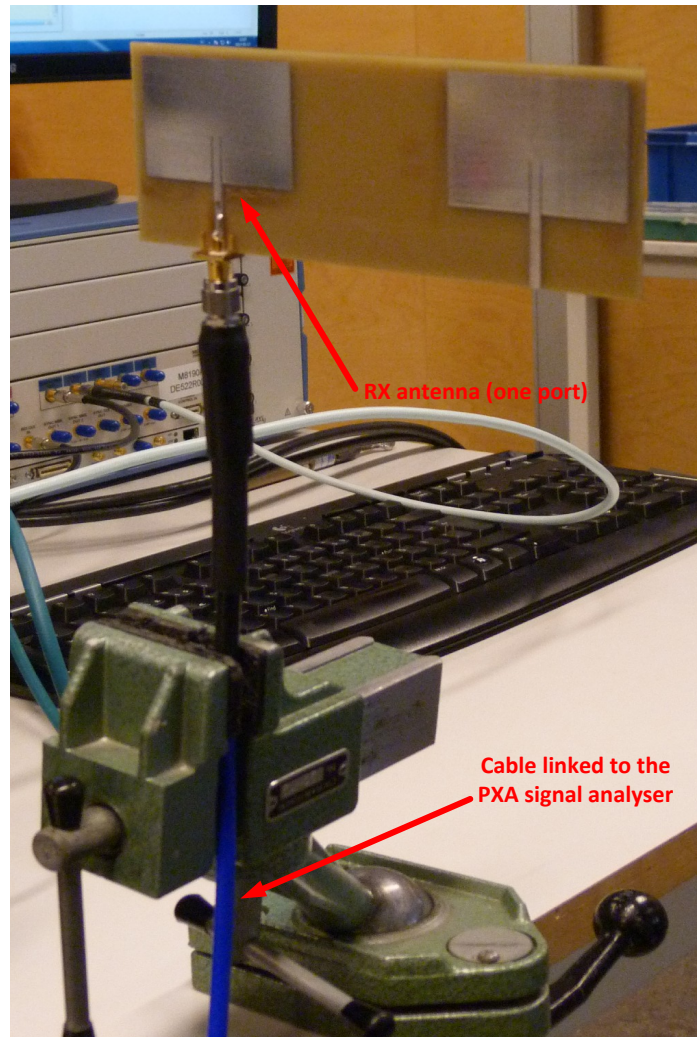


Figure D.2: Picture of the receiving antenna used in the measurement